

Unsupervised domain adaptation for radioisotope identification in gamma spectroscopy

Peter Lalor^{a,*}, Ayush Panigrahy^{a,b}, Alex Hagen^a

^a*Pacific Northwest National Laboratory, Richland, WA 99352 USA*

^b*University of Washington, Seattle, WA 98195 USA*

Abstract

Training machine learning models for radioisotope identification using gamma spectroscopy remains an elusive challenge for many practical applications, largely stemming from the difficulty of acquiring and labeling large, diverse experimental datasets. Simulations can mitigate this challenge, but the accuracy of models trained on simulated data can deteriorate substantially when deployed to an out-of-distribution operational environment. In this study, we demonstrate that unsupervised domain adaptation (UDA) can improve the ability of a model trained on synthetic data to generalize to a new testing domain, provided unlabeled data from the target domain is available. Conventional supervised techniques are unable to utilize this data because the absence of isotope labels precludes defining a supervised classification loss. We compare a range of different UDA techniques, finding that feature alignment strategies, particularly via maximum mean discrepancy (MMD) minimization or domain-adversarial training, yield the most consistent improvement to testing scores. For instance, using a custom transformer-based neural network, we achieve a testing accuracy of 0.904 ± 0.022 on an experimental LaBr_3 test set after performing unsupervised feature alignment via MMD minimization, compared to 0.754 ± 0.014 before alignment. Overall, our results highlight the potential of using UDA to adapt a radioisotope classifier trained on synthetic data for real-world deployment.

Keywords: Domain Adaptation, Transformer, Neural Network, Gamma Spectroscopy

1. Introduction

Improvements to the current performance of gamma spectroscopy are still sought in many applications, especially those with low signal-to-noise ratios (SNRs). Very recent papers cite the need for gamma spectroscopic improvements for mobile source search [1], nuclear facility upset detection [2], and national security missions [3] among others. Many current papers, such as those cited above, focus on improvements to the analysis applied to the data obtained from modern hardware, rather than on improvements to the hardware itself. The abundance of detectable photons from natural surroundings interferes with photons emitted from the source of interest across many situations—a problem which cannot be resolved by different hardware. This problem is analogous to standard problems in computer vision (CV) and natural language processing (NLP), where noise (pixels of unimportant objects in CV or stopwords in NLP) interferes with the signal (pixels of the object of interest in CV or key words conveying meaning in NLP). Unlike in CV and NLP, overparameterized machine learning has thus far evaded widespread adoption in the field of gamma spectroscopy.

*Corresponding author

Email address: peter.lalor@pnnl.gov

Telephone: (925) 453-1876

All three fields have challenges associated with training reliable, generalizable, and explainable models, but the solutions to those challenges from CV and NLP have not been applied to gamma spectroscopy. This is because of the lack of availability of suitable datasets for model training, since collecting and labeling sufficient experimental data is expensive and time-consuming, while relying on synthetic data is inherently limited by the sim-to-real gap [4].

Gamma spectroscopy, especially since the advent of portable spectroscopy detectors in the 1950s [5], is one of the most widely used radiation-detection disciplines. The relative ease of detection of photons compared to neutrons, and their relatively high penetration compared to beta and alpha radiation, lead to the ability to perform standoff detection of radiation sources. This standoff detection is useful in radiation safety, national security, and physical science applications. Additionally, the information conveyed by those photons' energy informs the composition of the source, which is useful in material characterization and forensics applications. Gamma spectrometers themselves have differing efficiency, resolution, and portability characteristics; however, they all display a convolution between the energy of the incident photon across the whole spectrum of detected energy. This is irreducible as it originates in the partial deposition of energy during the interaction of photons with matter, and causes challenges in detection and identification scenarios. Further, many natural materials exhibit photon emission, which leads to an ever-present rate of background photon detection events. These two complicating factors may be mitigated through hardware changes, but require advanced analytics for full resolution.

Thus, advanced analytics like machine learning are not new to the field of gamma spectroscopy. Analysis methods have been developed with increasing levels of sophistication, sometimes preceding other fields. For example, automated peak-finding algorithms were proposed as early as 1967 [6] and deployed in commercial software packages by 2006 [7]; whereas the first algorithm for its computer vision analog, object detection, was not proposed until 2006 [8, 9]. Unconstrained optimization-based curve fitting, the mathematical method which forms the basis for modern neural-network-based machine learning, was developed for the analysis of radiation spectra and reached mainstream (physics) software packages more than 30 years ago [10]. Only recently, and only in terrestrial applications¹, has gamma spectroscopy lagged CV and NLP on its adoption of cutting-edge machine learning techniques.

Machine learning and its applications to CV and NLP changed dramatically in 2012 with the success of AlexNet for classification of images from the ImageNet dataset [12]. The key insight leading to that success was that highly over-parameterized functions called neural networks could be optimized on large datasets to minimize the error on prediction tasks. Since then, parameterization has been a key determinant of machine learning success, and in fact “scaling-laws” which depend on the number of parameters of the model have since emerged [13, 14]. Parameter scaling in gamma spectroscopic analysis has not kept pace with that in CV and NLP. In fact, only some recent publications [4, 15, 16, 17] have embraced the over-parameterized machine learning paradigm.

This slow adoption is likely due to the lack of labeled data in gamma spectroscopy. AlexNet was enabled by the enormous ImageNet dataset, and the aforementioned scaling laws depend on the size of the data as well as the number of parameters in the model. Here again, CV and NLP have developed techniques that could be applicable to gamma spectroscopy, notably domain-adaptation and pretraining. Domain-adaptation has been complementary or competitive with pretraining techniques, largely used to supplement

¹High-energy physics and cosmology have led CV and NLP on analytics development (e.g., graph neural network architectures in track reconstruction using detection events [11]).

models displaying a generalization gap such as CV models trained on natural imagery transferring to overhead imagery [18]. In CV and NLP, self-supervised or semi-supervised pretraining is used to utilize vast amounts of unlabeled data available from scraped internet sources, and is used in most modern Large Language Models and Vision Language Models [19, 20, 21, 22, 23]. Especially with the sim-to-real gap identified in gamma spectroscopy [4], and the lack of consensus over the use of simulated data in other applied data science fields [24, 25], it is important to explore various options for domain adaptation or pretraining-based generalization improvement in gamma spectroscopy. This work presents such a study.

2. Background

2.1. Domain Shift

Domain adaptation for gamma spectroscopy is formalized as follows: we define $P_s(x, y)$ as the joint data-label probability distribution for a gamma spectrum x with label y for the source domain, and likewise $P_t(x, y)$ for the target domain. Our machine learning objective is to train a neural network classifier $h : \mathcal{X} \rightarrow \Delta^K$ to approximate $P_t(y | x)$ – that is, for a given spectrum x from the target domain, we aim to compute the most likely isotopic label y .

Lacking labels from the target domain, we might instead train h using labeled source-domain samples to approximate $P_s(y | x)$ with the hope that $P_s(y | x) \approx P_t(y | x)$ and thus the model trained on source-domain data can be used to classify target-domain spectra. However, in practice this is rarely effective due to the *domain shift* between source and target domains, which can be broadly categorized in the following types [26, 27]:

Covariate Shift occurs when the underlying distribution of spectra changes between source and target domain even if the mapping from gamma energy spectrum to isotopic labels remains unchanged. For instance, the target domain might contain more shielded examples than the source domain or fewer spectra with low noise. Formally, pure covariate shift occurs when $P_s(x) \neq P_t(x)$ while $P_s(y | x) = P_t(y | x)$.

Prior Shift occurs when the distribution of isotopic labels differs between source and target domain, even if each isotope produces the same distribution of spectra. For instance, the source domain might contain an equal number of every isotope, whereas the target domain contains a class imbalance. Formally, pure prior shift occurs when $P_s(y) \neq P_t(y)$ while $P_s(x | y) = P_t(x | y)$.

Concept Shift occurs when the fundamental relationship between isotopic label and spectral shape is different between source and target domains. For instance, the source and target domain could have a different geometry, background, gain drift, or detector response. Formally, concept shift occurs when $P_s(x | y) \neq P_t(x | y)$. This is the most difficult to fix using UDA techniques, since label-agnostic feature alignment typically requires that concept shift is small.

2.2. Model Architecture

Past literature in gamma spectroscopy implements a range of different machine learning architectures, including multilayer perceptrons (MLPs) [28, 29, 30] and convolutional neural networks (CNNs) [31, 32, 33, 34, 35] to more recent transformer-based neural networks (TBNNs) [36, 4]. We include a summary of each architecture below:

Multilayer Perceptrons represent a gamma spectrum as a 1D list of features and contain one or more hidden layers. In each layer, the features undergo a dense linear transformation followed by a nonlinear activation. MLPs are popular due to their simplicity and flexibility, but lack explicit spatial inductive bias. As a result, MLPs might struggle to learn local structure and are more likely to generalize poorly to spectra with different energy calibrations.

Convolutional Neural Networks implement a sliding 1D convolutional kernel across a gamma spectrum, calculating the dot product between the kernel weights and the local spectrum patch. This process captures spatial structure more efficiently than MLPs, but the locality is limited to nearby energy bins, meaning CNNs can be less effective at capturing long-range correlations across a gamma spectrum.

Transformer-based Neural Networks leverage the attention mechanism, first introduced in Ref. [19], to compute weights between different regions, or “patches,” of a spectrum. This enables TBNNs to capture long range correlations in a gamma spectrum, such as multiple decays from different nuclear energy levels. However, transformers are more complex to tune and suffer from quadratic scaling with number of spectral patches.

Transformers were first applied to gamma spectroscopy by Ref. [36], henceforth TBNN (Li *et al.*). More recent work introduced a more general transformer architecture with learnable patch embeddings and a [CLS] token, among other enhancements [4]. In the present work, we build upon this framework with TBNN-LinEmb and TBNN-NonlinEmb, comparing a single affine projection (i.e., one fully connected layer) to a one-hidden-layer MLP embedder. Furthermore, we use a global average pooling readout instead of a learnable [CLS] token, better matching spectrum-level classification by aggregating evidence across all channels.

Beyond these architectures, past research has also explored autoencoder-based anomaly detection [17, 15], recurrent neural networks for source identification [17], and custom semi-supervised networks for radioisotope proportion estimation and out-of-distribution identification [37]. Given the more specialized nature of these methods, we focus the architectural analysis of the present work to MLPs, CNNs, and TBNNs.

2.3. Unsupervised Domain Adaptation Methods

In this analysis, we consider the setting where we have access to a labeled *source domain* and an unlabeled *target domain*. The source domain $\mathcal{D}_s = \{(x_i^s, y_i^s)\}_{i=1}^{n_s}$ consists of n_s labeled spectra drawn from $P_s(x, y)$, and the target domain $\mathcal{D}_t = \{x_j^t\}_{j=1}^{n_t}$ consists of n_t spectra drawn from $P_t(x)$ for which labels are not available during training. We first pretrain a *source-only* model using the labeled source domain \mathcal{D}_s , writing our model as the composition $h_{\theta, \phi} = g_\phi \circ f_\theta$, where $f_\theta : \mathcal{X} \rightarrow \mathbb{R}^d$ is the feature extractor and $g_\phi : \mathbb{R}^d \rightarrow \Delta^K$ is the classifier. Here, we represent the feature extractor as the entire neural network up to (and including) the penultimate layer, and the classifier as the final dense classification head. We thus write the source-only pretraining objective as follows:

$$\min_{\theta, \phi} \mathcal{L}_{\text{src}}(\theta, \phi) = \frac{1}{n_s} \sum_{i=1}^{n_s} \ell(g_\phi(f_\theta(x_i^s)), y_i^s) , \quad (1)$$

where $\ell(\cdot, \cdot)$ is the cross-entropy loss. After pretraining a source-only model by minimizing Eq. 1, we consider various UDA methods (Sections 2.3.1–2.3.7) which introduce a modified training objective to encourage alignment between feature distributions $f_\theta(\mathcal{D}_s)$ and $f_\theta(\mathcal{D}_t)$ using unlabeled target samples from \mathcal{D}_t . All of the following UDA algorithms were implemented from scratch using TensorFlow [38].

2.3.1. Adversarial Discriminative Domain Adaptation (ADDA)

ADDA [39] trains a new feature extractor f_{θ_t} to produce target-domain features which match the source feature distribution (i.e., $f_{\theta_t}(\mathcal{D}_t) \approx f_{\theta}(\mathcal{D}_s)$). This is accomplished by fixing the source feature extractor and adversarially training a target feature extractor f_{θ_t} and domain discriminator $d_{\psi} : \mathbb{R}^d \rightarrow (0, 1)$. The domain discriminator’s objective is to identify whether a feature vector originated from a source-domain spectrum (0) or a target-domain spectrum (1), trained via the following:

$$\max_{\psi} \mathbb{E}_{x_s \sim \mathcal{D}_s} [\log(1 - d_{\psi}(f_{\theta}(x_s)))] + \mathbb{E}_{x_t \sim \mathcal{D}_t} [\log d_{\psi}(f_{\theta_t}(x_t))] , \quad (2)$$

while the target feature extractor is trained to fool the discriminator:

$$\min_{\theta_t} \mathbb{E}_{x_t \sim \mathcal{D}_t} [-\log(1 - d_{\psi}(f_{\theta_t}(x_t)))] . \quad (3)$$

The final model is then written as the composition of the source classifier and the target feature extractor: $g_{\phi} \circ f_{\theta_t}$. This approach preserves the source-only model decision boundary while transforming target features to better align with the source domain.

2.3.2. Deep Adaptation Networks (DAN)

DAN [40] adds a term to the supervised source-only loss function to minimize the maximum mean discrepancy (MMD) between the source and target feature vectors $z_s = f_{\theta}(x_s)$ and $z_t = f_{\theta}(x_t)$. MMD is defined as the distance between the source and target feature embeddings in a reproducing kernel Hilbert space (RKHS), calculated using the kernel trick:

$$\text{MMD}^2(z_s, z_t) = \left\| \frac{1}{n_s} \sum_{i=1}^{n_s} \varphi(z_s^i) - \frac{1}{n_t} \sum_{j=1}^{n_t} \varphi(z_t^j) \right\|_{\mathcal{H}}^2 = \frac{1}{n_s^2} \sum_{i,i'} k(z_s^i, z_s^{i'}) + \frac{1}{n_t^2} \sum_{j,j'} k(z_t^j, z_t^{j'}) - \frac{2}{n_s n_t} \sum_{i,j} k(z_s^i, z_t^j) , \quad (4)$$

where k is a positive definite kernel and φ is its feature map. The DAN training objective is thus

$$\min_{\theta, \phi} \mathcal{L}_{\text{src}}(\theta, \phi) + \lambda \text{MMD}^2(z_s, z_t) , \quad (5)$$

where $\lambda \geq 0$ is a tradeoff parameter which balances the contribution of the source-only supervised term with the MMD feature alignment penalty. In our experiments, we compute MMD using a multi-kernel Gaussian radial basis function (RBF), averaging over several kernel bandwidths and omitting diagonal terms. The resulting domain-adapted model thus retains the ability to correctly classify source-domain spectra while simultaneously producing aligned source and target feature vectors, yielding better generalization to the target domain.

2.3.3. Domain Adversarial Neural Networks (DANN)

DANN [41] trains the source feature extractor to learn domain-invariant features. This is accomplished by training a domain discriminator $d_{\psi} : \mathbb{R}^d \rightarrow (0, 1)$ while adversarially updating the feature extractor to fool the discriminator. The min-max objective is thus:

$$\min_{\theta, \phi} \max_{\psi} \mathcal{L}_{\text{src}}(\theta, \phi) - \kappa \mathbb{E}_{x \sim (\mathcal{D}_s \cup \mathcal{D}_t)} [\ell_d(d_{\psi}(f_{\theta}(x)), r(x))] , \quad (6)$$

where $\kappa \geq 0$ is the domain-adversarial strength, $r(x) \in \{0, 1\}$ is the true domain label (0=source, 1=target), and $\ell_d(\cdot, \cdot)$ is the binary cross-entropy loss. In practice, Eq. 6 is optimized using a gradient

reversal layer that multiplies the gradient from the discriminator loss entering the feature extractor by $-\kappa$ during backpropagation. After domain adaptation, the feature extractor produces a domain-agnostic representation and is thus less likely to overfit to features only present in the source domain.

2.3.4. Deep Correlation Alignment (DeepCORAL)

DeepCORAL [42] aligns the second-order statistics of the source and target distributions by minimizing the difference between their covariance matrices. Defining covariances C_s and C_t for minibatch feature matrices $Z_s \in \mathbb{R}^{n_s \times d}$ and $Z_t \in \mathbb{R}^{n_t \times d}$ as:

$$C_s = \frac{1}{n_s - 1} (Z_s - \mathbf{1}\bar{z}_s^\top)^\top (Z_s - \mathbf{1}\bar{z}_s^\top), \quad C_t = \frac{1}{n_t - 1} (Z_t - \mathbf{1}\bar{z}_t^\top)^\top (Z_t - \mathbf{1}\bar{z}_t^\top), \quad (7)$$

we express the CORAL loss as:

$$\mathcal{L}_{\text{CORAL}} = \frac{1}{4d^2} \|C_s - C_t\|_F^2, \quad (8)$$

and subsequently optimize the network via the combined objective:

$$\min_{\theta, \phi} \mathcal{L}_{\text{src}}(\theta, \phi) + \lambda \mathcal{L}_{\text{CORAL}}, \quad (9)$$

where λ is a tradeoff parameter. The result is a simple and lightweight way to align source and target feature distributions.

2.3.5. Deep Joint Optimal Transport (DeepJDOT)

DeepJDOT [43] aligns the *joint* distributions of features and labels using optimal transport (OT). For each minibatch, a pairwise cost is defined as

$$c_{ij}(\theta, \phi) = \alpha \|f_\theta(x_s^i) - f_\theta(x_t^j)\|_2^2 + \beta \ell(g_\phi(f_\theta(x_t^j)), y_s^i), \quad (10)$$

where $\ell(\cdot, \cdot)$ is the cross-entropy loss. The first term in Eq. 10 measures the similarity between samples i and j in feature space, and the second term measures the agreement in label space between the *true* source label y_s and the *predicted* target label $\hat{y}_t = g_\phi(f_\theta(x_t^j))$. In Eq. 10, $\alpha, \beta \geq 0$ are hyperparameters which balance the feature-distance and label-consistency. We then compute a *soft matching* (transport plan) $\gamma \in \mathbb{R}_+^{n_s \times n_t}$ between the n_s source spectra and n_t target spectra by solving the entropic OT problem with uniform marginals using Sinkhorn iterations. We subsequently define the OT loss as follows:

$$\mathcal{L}_{\text{OT}}(\theta, \phi) = \sum_{i=1}^{n_s} \sum_{j=1}^{n_t} \gamma_{ij} c_{ij}(\theta, \phi). \quad (11)$$

Our training objective is thus:

$$\min_{\theta, \phi} \mathcal{L}_{\text{src}}(\theta, \phi) + \lambda \mathcal{L}_{\text{OT}}(\theta, \phi), \quad (12)$$

for a tradeoff parameter λ . Through this OT procedure, we achieve a class aware method of aligning source and target domains.

2.3.6. Mean Teacher

Mean Teacher [44] enforces predictive consistency under noise/augmentations between a *teacher* model and *student* model, where the weights of the teacher are an exponential moving average (EMA) of the student’s weights. For each target spectrum x_t , two stochastic views $x_t^{(s)}$ and $x_t^{(t)}$ are formed by adding Poisson noise to the original spectrum, with an *effective counts* hyperparameter introduced to control the

scale of the noise² We then define a self-supervised consistency loss as the mean squared error between the student’s predictions $g_{\phi_s}(f_{\theta_s}(x_t^{(s)}))$ and the teacher’s predictions $g_{\phi_t}(f_{\theta_t}(x_t^{(t)}))$:

$$\mathcal{L}_{\text{cons}}(\theta_s, \phi_s; \theta_t, \phi_t) = \mathbb{E}_{x_t \sim \mathcal{D}_t} \left[\left\| g_{\phi_s}(f_{\theta_s}(x_t^{(s)})) - g_{\phi_t}(f_{\theta_t}(x_t^{(t)})) \right\|_2^2 \right]. \quad (13)$$

The student parameters are optimized via the combined training objective:

$$\min_{\theta_s, \phi_s} \mathcal{L}_{\text{src}}(\theta_s, \phi_s) + \lambda \mathcal{L}_{\text{cons}}(\theta_s, \phi_s; \theta_t, \phi_t). \quad (14)$$

for a tradeoff parameter λ , and the teacher parameters are updated by EMA:

$$\theta_t \leftarrow \mu \theta_t + (1 - \mu) \theta_s, \quad \phi_t \leftarrow \mu \phi_t + (1 - \mu) \phi_s, \quad (15)$$

where $\mu \in [0, 1)$ is the EMA decay. Mean Teacher encourages stable predictions on target spectra while remaining robust to noise.

2.3.7. Simple Contrastive Learning (SimCLR)

SimCLR [46] performs self-supervised learning by contrasting two stochastic views of the same underlying spectrum. Similar to Mean Teacher, we perform independent Poisson resampling on each target spectrum x_t to generate two views $x_t^{(1)}$ and $x_t^{(2)}$. We subsequently introduce a projection head $q_\omega : \mathbb{R}^d \rightarrow \mathbb{R}^{d'}$ and compute $z_1 = q_\omega(f_\theta(x_t^{(1)}))$, $z_2 = q_\omega(f_\theta(x_t^{(2)}))$. For a minibatch of m target spectra, we define a contrastive InfoNCE loss as:

$$\mathcal{L}_{\text{NCE}} = \frac{1}{2} (\mathcal{L}_{1 \rightarrow 2} + \mathcal{L}_{2 \rightarrow 1}), \quad \mathcal{L}_{1 \rightarrow 2} = \frac{1}{m} \sum_{i=1}^m -\log \frac{\exp(\text{sim}(z_1^i, z_2^i)/\tau)}{\sum_{j=1}^m \exp(\text{sim}(z_1^i, z_2^j)/\tau)} \quad (16)$$

where $\text{sim}(u, v) = \frac{u^T v}{\|u\| \|v\|}$ is the cosine similarity and $\tau > 0$ is a temperature hyperparameter. The overall training objective is thus:

$$\min_{\theta, \phi, \omega} \mathcal{L}_{\text{src}}(\theta, \phi) + \lambda \mathcal{L}_{\text{NCE}}(\theta, \omega), \quad (17)$$

where $\lambda \geq 0$ is a tradeoff parameter. SimCLR encourages a model to learn augmentation-invariant representations of target spectra while retaining the ability to correctly classify source spectra.

3. Methodology

3.1. Dataset Curation

In this analysis, we consider three domain adaptation scenarios, summarized in Table 1. In the first domain adaptation scenario, *sim-to-sim*, our target domain is simulated in **Geant4**, an open-source Monte Carlo simulation package for modeling the passage of radiation through matter [47, 48]. We simulated high-resolution spectra for 55 radioisotopes, placing each in a cylindrical sample container, and measuring incoming gamma rays using a high-purity germanium (HPGe) detector placed one meter from the source, mirroring the geometry from Ref. [49]. Five representative detector geometries and five source-container configurations

²Alternative data augmentations are possible, such as background addition, detector broadening, peak masking, or gain shift [45]. We selected Poisson resampling to serve as a simple baseline.

Table 1: Summary of the datasets used in this study.

Scenario	Domain	Acquisition Mode	Isotopic Composition	Number of Isotopes	Size
sim-to-sim (HPGe)	Source	GADRAS	Mixed	55	1.3×10^6
	Target	Geant4	Mixed	55	1.3×10^6
sim-to-real (LaBr ₃)	Source	GADRAS	Single	32	1.4×10^6
	Target	Experiment	Single	32	15,091
sim-to-real (NaI(Tl))	Source	GADRAS	Single	32	1.4×10^6
	Target	Experiment	Single	32	10,440

(aluminum, thorium, cellulose nitrate, water, and copper) were used to capture a range of realistic counting scenarios. These template spectra are then mixed, background-added, and Poisson resampled using PyRIID, a Python package for gamma spectral synthesis [50]. The resulting dataset is class-balanced and comprises exclusively solid isotopes, with SNRs log-uniformly sampled between 100 and 1000. Each spectrum contains up to 14 isotopes, with relative source contributions drawn from a Dirichlet distribution ($\alpha = 3$).

The second and third domain adaptation scenarios, *sim-to-real*, reflect a different measurement scenario from the sim-to-sim simulations. Our target domain consists of experimental spectra measured using handheld sodium iodide (NaI(Tl)) and lanthanum bromide (LaBr₃) detectors, respectively, measured in standardized source-shield configurations (none, steel, lead, polyethylene). The spectra were interpolated onto a uniform 1024-bin energy grid from 0 to 3000 keV, and each source belonged to one of 32 isotope classes (partially overlapping the sim-to-sim isotopes). Due to data sensitivity constraints, detailed information about the sim-to-real experimental datasets (e.g., specific isotope lists or acquisition protocols) is not available for public release.

For each domain adaptation scenario, we also simulated a corresponding source-domain dataset using GADRAS. GADRAS is a semi-empirical detector response calculation software which couples deterministic attenuation calculations with precomputed response functions to quickly generate synthetic template spectra [51]. These high resolution template spectra are then mixed (sim-to-sim only), background-added, and Poisson resampled using PyRIID to efficiently generate a large dataset for machine learning training. For the sim-to-sim dataset, the SNR was sampled log-uniformly between 100 and 1000. For the sim-to-real datasets, the SNR was instead drawn from an exponential distribution, with a mean of 896 for LaBr and 1370 for NaI. All source-domain datasets were class-balanced, and the dataset curation process is described in further detail in our previous research [4].

The datasets were partitioned into training, validation, and testing with a 70/15/15 split. Splits were performed randomly rather than stratified by class, and all reported results correspond to a single fixed split. In all three domain adaptation scenarios, the isotopic labels of the target domain spectra were masked to imitate a setting where ground truth composition is unknown. The isotopic labels of the validation and testing sets were not masked in order to evaluate the performance of trained models for algorithmic comparison.

The three scenarios considered in this analysis differ not only in the nature of the domain shift (sim-to-sim versus sim-to-real), but also in task structure. The sim-to-sim scenario contains 55 isotope classes, and each spectrum contains an arbitrary mixture of up to 14 isotopes, while the sim-to-real scenarios involve

single-label classification over a partially overlapping subset of 32 isotope classes. These scenarios are thus not intended as direct comparisons against each other, but rather as independent evaluations of UDA across a wide range of settings in gamma spectroscopy. We note that the two sim-to-real scenarios (LaBr₃ and NaI(Tl)) are well-matched to each other (same 32 isotopes and single-isotope task) and differ only in detector type, so cross-comparison between those two is well-controlled.

3.2. Model Training

As an input preprocessing step, we applied a variance-stabilizing square-root transform to the raw channel counts, $\tilde{x} = \sqrt{x}$. We subsequently z -score normalized the transformed counts on a per-spectrum basis, $\hat{x} = (\tilde{x} - \mu)/\sigma$, where μ and σ are the mean and standard deviation of \tilde{x} computed across channels for a single spectrum. We found this preprocessing improved training stability, especially for the transformer architectures.

To train the source-only models, we first performed a Bayesian hyperparameter search using the `Optuna` software package [52]. For each architecture, we performed 100 Bayesian trials with a validation loss search criterion. For consistency, we used the same architecture hyperparameters across all scenarios (selected as the best source-only parameters from the sim-to-sim dataset), but training hyperparameters (learning rate, batch size, weight decay, dropout) were calculated separately for every run. Once the best hyperparameters were selected, we trained 10 models using different random weight initializations, per-epoch data shuffling, and dropout seeds. This ensemble technique was chosen as a simple form of uncertainty estimation, as the 1σ sample standard deviation of metric evaluations across the 10 randomized trials quantifies realistic run-to-run performance fluctuations.

After source-only models were trained, we performed an additional 100 Bayesian trials to determine the best UDA-specific hyperparameters. We performed this search independently for each architecture (Section 2.2) and for each UDA method (Section 2.3). Once the best hyperparameters were selected, we again trained 10 models using different random seeds to estimate uncertainty in model performance. The domain-adapted models and source-only models were paired by using the corresponding source-only model as the initial configuration prior to unsupervised domain alignment. We include a summary of the selected hyperparameters for each domain adaptation scenario across all architectures and UDA methods in Tables A.5–A.13.

4. Results

4.1. Domain Shift Characterization

To illustrate the presence of source-to-target domain shift for each of the domain adaptation scenarios, we computed three domain-gap metrics. First, we trained a linear feature-space domain discriminator $d_\psi : \mathbb{R}^d \rightarrow (0, 1)$ to identify whether a feature vector $z_{s,t} = f_\theta(x_{s,t})$ originated from the source-domain (0) or target-domain (1). We also trained an input-space domain discriminator directly on $x_{s,t}$. We subsequently computed the area under the receiver operating characteristic curve (AUROC) on a held-out test set to quantify how easily each domain discriminator was able to differentiate between source and target domains (AUROC = 0.5 \implies random guessing, AUROC = 1 \implies perfect domain discrimination) [53]. We supplemented this analysis by empirically estimating the MMD (Eq. 4) between source and target ℓ_1 -normalized spectra using an RBF kernel with median heuristic bandwidth (MMD = 0 \implies identical distributions, larger values indicate larger domain gap) [54]. Finally, we defined a class-conditional expected pairwise Wasserstein distance as the average Wasserstein-1 distance $W_1(\cdot, \cdot)$ between random ℓ_1 -normalized spectra for a given isotopic label

Scenario	AUROC (features)	AUROC (inputs)	MMD ²	R
sim-to-sim (HPGe)	[0.993, 0.996]	[0.957, 0.967]	[2.74, 2.93]	[1.36, 1.40]
sim-to-real (LaBr ₃)	[0.982, 0.988]	[0.852, 0.874]	[2.26, 2.55]	[1.87, 1.93]
sim-to-real (NaI(Tl))	[0.983, 0.989]	[0.780, 0.808]	[1.30, 2.53]	[1.93, 1.99]

Table 2: 95% CI for each domain separability metric, indicating a statistically significant domain gap between source and target domains for all domain adaptation scenarios.

c [55]. We then compute a custom heuristic R by comparing the source-to-target class-conditional expected pairwise Wasserstein distance to the same distance evaluated within each domain:

$$R(\mathcal{D}_s, \mathcal{D}_t) := \frac{\sum_{c=1}^K \widetilde{W}_{s,t}^{(c)}}{\frac{1}{2} \sum_{c=1}^K (\widetilde{W}_{s,s}^{(c)} + \widetilde{W}_{t,t}^{(c)})}, \quad \widetilde{W}_{s,t}^{(c)} := \mathbb{E}_{\substack{x_s \sim \mathcal{D}_s^c \\ x_t \sim \mathcal{D}_t^c}} [W_1(x_s, x_t)]. \quad (18)$$

Intuitively, we interpret the Wasserstein distance $W_1(\cdot, \cdot)$ between two spectra as the minimal transport cost to morph one spectrum into another, and R as the ratio of between-domain to within-domain spectral dissimilarity. Thus $R = 1 \implies$ consistency between \mathcal{D}_s and \mathcal{D}_t , whereas $R \gg 1 \implies$ substantial dissimilarity. We compute Eq. 18 in the sim-to-sim scenario using single-isotope (one-hot) spectra from both the source and target datasets, since mixed spectra cannot be uniquely assigned to a single class c . For each domain separability metric, we computed a 95% confidence interval (CI) using a stratified bootstrapping approach, and performed statistical significance testing via an approximate bootstrap for AUC (null = 0.5) and R (null = 1) and a permutation test for MMD (null = 0). These results are summarized in table 2, where we see that all three metrics identify a statistically significant source-to-target domain gap across all domain adaptation scenarios. This result highlights the importance of leveraging domain adaptation techniques to reduce the impact of domain shift on model generalizability.

4.2. Testing Scores

The results of this analysis are summarized in Table 3, where we compare the performance of different machine learning models on a held-out testing dataset, with 1σ uncertainties calculated as the sample standard deviations across the 10 randomized trials described in Section 3.2. In the sim-to-real scenarios, we compute the accuracy on the held-out experimental testing dataset as our evaluation metric. In the sim-to-sim scenario, we instead use the APE score [4] as our evaluation metric, calculated via Eq. 19. The APE score provides a simple, bounded $[0, 1]$ agreement metric (0=maximal deviation, 1=perfect reconstruction) to describe how precisely a model reconstructs the mixed isotopic composition of a heterogeneous source.

$$\text{APE}(h_{\theta,\phi}; \mathcal{D}_{\text{test}}) := 1 - \frac{1}{2n_{\text{test}}} \sum_{i=1}^{n_{\text{test}}} \|\hat{y}_i - y_i\|_1, \quad \hat{y}_i := h_{\theta,\phi}(x_i) \in \Delta^K, \quad y_i \in \Delta^K. \quad (19)$$

We also include a ‘‘Train on Target’’ row in Table 3, indicating the performance of a model trained directly on a labeled target-domain dataset, serving as a theoretical upper bound on model performance and included only for reference. We remark that Train on Target = 1 for the sim-to-real scenarios, stemming from the single-label, high SNR nature of the dataset. While a more complicated experimental dataset is desirable, we still expect the results of this research to apply broadly and suggest analysis using more challenging datasets as an avenue for future work.

We observe mixed results in the sim-to-sim scenario. The most consistent performance gain compared to source-only were the DANN models, where the MLP achieved an APE score of 0.649 ± 0.004 (compared to 0.623 ± 0.002 of source-only), TBNN (Li *et al.*) achieved an APE score of 0.690 ± 0.005 (compared to 0.630 ± 0.003 of source-only), TBNN-LinEmb achieved an APE score of 0.691 ± 0.006 (compared to 0.653 ± 0.004 of source-only), and TBNN-NonlinEmb achieved an APE score of 0.697 ± 0.006 (compared to 0.668 ± 0.005 of source-only). DAN and ADDA yielded similar improvements, although the performance gain was only seen using the three transformer architectures. None of the UDA methods improved performance using a CNN backbone.

In the sim-to-real dataset, we observe a stronger result. Across all architectural backbones, the best UDA model achieves an average classification accuracy improvement of 14.9 percentage points relative to the source-only model. DANN and DAN yielded the strongest average improvement except when using a CNN backbone, in which case DeepCORAL was best. Using the LaBr₃ testing set, the DAN MLP achieved an accuracy of 0.895 ± 0.018 (versus 0.743 ± 0.010 source-only), DeepCORAL CNN achieved 0.937 ± 0.021 (versus 0.800 ± 0.019 source-only), DANN TBNN (Li *et al.*) achieved 0.932 ± 0.022 (versus 0.775 ± 0.010 source-only), DAN TBNN-LinEmb achieved 0.904 ± 0.022 (versus 0.754 ± 0.014 source-only), and DANN TBNN-NonlinEmb achieved 0.934 ± 0.022 (versus 0.765 ± 0.013 baseline).

To statistically support these results, we performed a series of one-sided Wilcoxon signed-rank tests testing the null hypothesis that UDA provides no significant improvement to testing scores compared to the source-only models. We chose a Wilcoxon signed-rank test due to the nature of having paired data (each source-only model was used as the initial configuration for the UDA run) and because the test makes no assumptions regarding the normality of differences. We present the results in Table A.14 for all three domain adaptation scenarios. In the sim-to-sim scenario, the domain-adapted models achieve statistically superior performance to the source-only models in 13 out of 35 comparisons, while in the sim-to-real scenarios, the domain-adapted models achieve statistically superior performance to the source-only models in 30 out of 35 comparisons for the LaBr₃ detector and 27 out of 35 for the NaI(Tl) detector. In particular, using a transformer model (TBNN (Li *et al.*), TBNN-LinEmb, or TBNN-NonlinEmb) with either DAN or DANN for domain adaptation provides a statistically significant improvement over source-only for every comparison across all domain adaptation scenarios.

4.3. Latent Representation Analysis

To interpret the impact of UDA on model behavior, we visualized the extracted feature representations of source- and target-domain spectra using uniform manifold approximation and projection (UMAP) [56]. We show the results using a TBNN-LinEmb architecture for the sim-to-sim scenario in Figs. 1a (source) and 1b (DANN), where we clearly see that the domain adaptation step results in qualitatively better alignment between the extracted source features and target features. Despite the apparent geometric alignment, our results from Section 4.2 suggest that the improvement to testing APE score is relatively minor (source-only APE = 0.653 ± 0.004 , DANN APE = 0.691 ± 0.006). In the sim-to-real scenarios, our observations are almost the opposite: Figs. 1c–1f reveal that UDA does not drastically improve qualitative feature alignment. We see strong clustering of both synthetic and experimental features, and it is difficult to articulate improved cluster alignment after domain adaptation. Despite this, we observe substantial double-digit improvements to testing accuracy (source-only accuracy = 0.754 ± 0.014 , DANN accuracy = 0.898 ± 0.032). For reference, we include the same visualizations for other UDA architectures in Fig. A.3 (sim-to-sim HPGe), Fig. A.4 (sim-to-real LaBr₃), and Fig. A.5 (sim-to-real NaI(Tl)).

Table 3: Evaluation metric scores on the target-domain test dataset for seven different UDA techniques. The ‘‘Source-only’’ row indicates models that were only trained on source-domain data with no domain adaptation step, serving as a baseline. The ‘‘Train on Target’’ row indicates models that were trained on labeled target-domain data, serving as a theoretical best-case scenario. Cell entries are calculated as the mean and sample standard deviation across 10 random trials. The best performing method for each architecture (excluding ‘‘Train on Target’’) is highlighted in bold.

(a) Scenario: sim-to-sim (HPGe). Cell entries indicate testing APE score

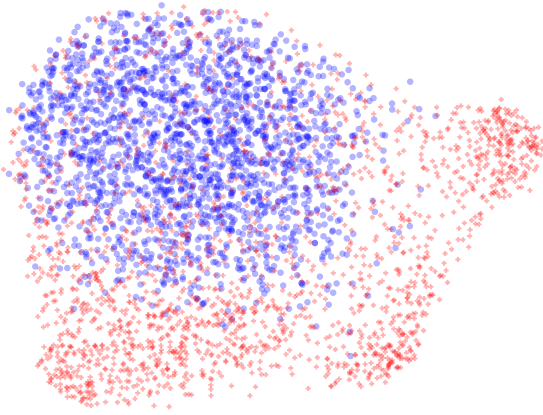
	MLP	CNN	TBNN (Li <i>et al.</i>)	TBNN-LinEmb	TBNN-NonlinEmb
Source-only	0.623 \pm 0.002	0.635 \pm 0.001	0.630 \pm 0.003	0.653 \pm 0.004	0.668 \pm 0.005
ADDA	0.604 \pm 0.012	0.614 \pm 0.018	0.667 \pm 0.007	0.678 \pm 0.009	0.688 \pm 0.008
DAN	0.592 \pm 0.004	0.607 \pm 0.003	0.659 \pm 0.005	0.667 \pm 0.004	0.691 \pm 0.005
DANN	0.649 \pm 0.004	0.630 \pm 0.012	0.690 \pm 0.005	0.691 \pm 0.006	0.697 \pm 0.006
DeepCORAL	0.629 \pm 0.002	0.619 \pm 0.012	0.641 \pm 0.012	0.640 \pm 0.009	0.650 \pm 0.006
DeepJDOT	0.390 \pm 0.185	0.614 \pm 0.005	0.631 \pm 0.005	0.626 \pm 0.004	0.609 \pm 0.011
Mean Teacher	0.484 \pm 0.014	0.573 \pm 0.009	0.589 \pm 0.112	0.633 \pm 0.016	0.612 \pm 0.026
SimCLR	0.573 \pm 0.005	0.605 \pm 0.007	0.649 \pm 0.004	0.605 \pm 0.006	0.648 \pm 0.009
Train on Target	0.896 \pm 0.001	0.881 \pm 0.001	0.891 \pm 0.001	0.895 \pm 0.001	0.889 \pm 0.001

(b) Scenario: sim-to-real (LaBr₃). Cell entries indicate testing accuracy

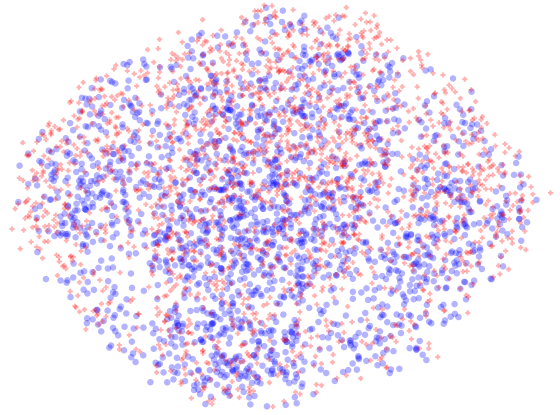
	MLP	CNN	TBNN (Li <i>et al.</i>)	TBNN-LinEmb	TBNN-NonlinEmb
Source-only	0.743 \pm 0.010	0.800 \pm 0.019	0.775 \pm 0.010	0.754 \pm 0.014	0.765 \pm 0.013
ADDA	0.807 \pm 0.039	0.868 \pm 0.014	0.836 \pm 0.036	0.821 \pm 0.044	0.826 \pm 0.036
DAN	0.895 \pm 0.018	0.841 \pm 0.028	0.901 \pm 0.027	0.904 \pm 0.022	0.878 \pm 0.019
DANN	0.879 \pm 0.029	0.926 \pm 0.016	0.932 \pm 0.022	0.898 \pm 0.032	0.934 \pm 0.022
DeepCORAL	0.796 \pm 0.028	0.937 \pm 0.021	0.853 \pm 0.017	0.876 \pm 0.026	0.854 \pm 0.024
DeepJDOT	0.747 \pm 0.015	0.818 \pm 0.020	0.800 \pm 0.032	0.830 \pm 0.038	0.849 \pm 0.030
Mean Teacher	0.757 \pm 0.010	0.773 \pm 0.032	0.866 \pm 0.026	0.746 \pm 0.013	0.785 \pm 0.021
SimCLR	0.837 \pm 0.014	0.869 \pm 0.010	0.868 \pm 0.040	0.840 \pm 0.032	0.853 \pm 0.030
Train on Target	1.000 \pm 0.000	1.000 \pm 0.000	1.000 \pm 0.000	1.000 \pm 0.000	1.000 \pm 0.000

(c) Scenario: sim-to-real (NaI(Tl)). Cell entries indicate testing accuracy

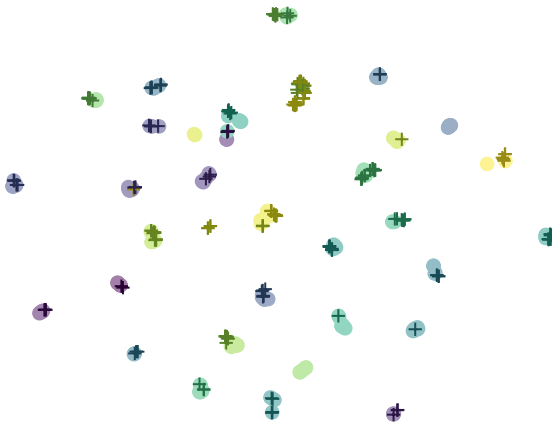
	MLP	CNN	TBNN (Li <i>et al.</i>)	TBNN-LinEmb	TBNN-NonlinEmb
Source-only	0.748 \pm 0.011	0.818 \pm 0.027	0.761 \pm 0.012	0.749 \pm 0.018	0.742 \pm 0.015
ADDA	0.841 \pm 0.034	0.847 \pm 0.050	0.851 \pm 0.030	0.828 \pm 0.035	0.739 \pm 0.050
DAN	0.853 \pm 0.028	0.833 \pm 0.034	0.933 \pm 0.025	0.905 \pm 0.023	0.910 \pm 0.029
DANN	0.888 \pm 0.027	0.853 \pm 0.037	0.924 \pm 0.022	0.898 \pm 0.037	0.921 \pm 0.023
DeepCORAL	0.797 \pm 0.031	0.895 \pm 0.025	0.877 \pm 0.027	0.881 \pm 0.027	0.870 \pm 0.029
DeepJDOT	0.802 \pm 0.016	0.798 \pm 0.035	0.852 \pm 0.030	0.875 \pm 0.026	0.882 \pm 0.042
Mean Teacher	0.739 \pm 0.015	0.759 \pm 0.032	0.906 \pm 0.018	0.776 \pm 0.034	0.785 \pm 0.023
SimCLR	0.841 \pm 0.019	0.861 \pm 0.026	0.930 \pm 0.016	0.849 \pm 0.037	0.832 \pm 0.041
Train on Target	1.000 \pm 0.000	1.000 \pm 0.000	1.000 \pm 0.000	1.000 \pm 0.000	1.000 \pm 0.000



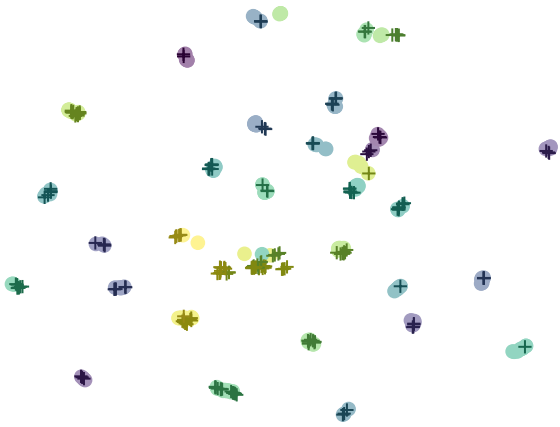
(a) Sim-to-sim HPGe scenario, source-only model.



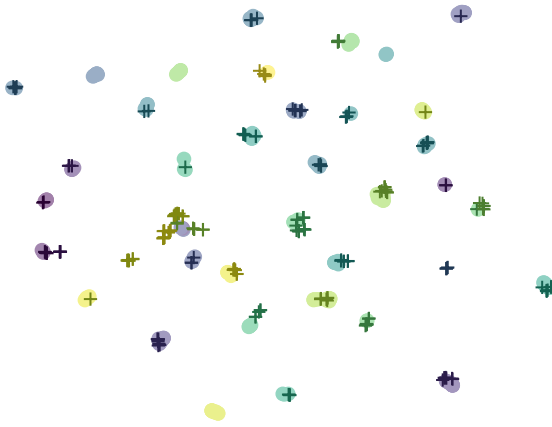
(b) Sim-to-sim HPGe scenario, DANN model.



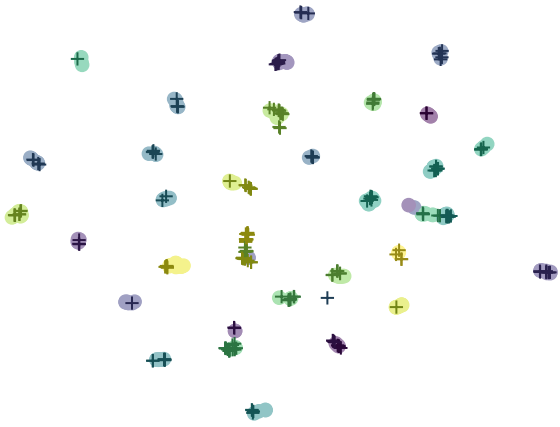
(c) Sim-to-real LaBr₃ scenario, source-only model.



(d) Sim-to-real LaBr₃ scenario, DANN model.



(e) Sim-to-real NaI(Tl) scenario, source-only model.



(f) Sim-to-real NaI(Tl) scenario, DANN model.

Figure 1: UMAP visualizations of the feature extractor outputs for source spectra ('o' markers) and target spectra ('+' markers) using a TBNN-LinEmb architecture. In the sim-to-sim scenario (top row), color indicates domain (blue = source, red = target). In the sim-to-real scenarios (middle and bottom rows), color indicates class, which is possible because the sim-to-real data is single-label.

4.4. Model Diagnostics

To better understand the performance of our models, we consider a wide range of literature-grounded diagnostic measurements. **Accuracy** measures the fraction of correctly classified testing spectra, and **Negative log-likelihood** [57] reports the average negative log-probability assigned to the true class. **Brier score** [58] measures the mean squared error between predicted probabilities and one-hot labels, and **Expected calibration error** [59] calculates the average absolute difference between accuracy and confidence across probability bins. **Prediction margin mean (p10)** [60] measures the mean (10th) percentile of the log-probability margin between true and best alternative class, and **AUROC (entropy)** evaluates the ability of predictive uncertainty to identify misclassified examples using the area under the receiver operating characteristic of the uncertainty score [61]. **Mean Jacobian norm** measures input sensitivity by calculating the mean squared ℓ_2 norm of the loss gradient with respect to the normalized spectral inputs [62]. Lastly, we construct a k -nearest-neighbor (k -NN) graph of the input spectra and compute the following metrics: [63, 64] (i) **k -NN TV Hard** is the fraction of k -NN edges with differing predicted class labels, (ii) **k -NN prob ℓ_2** is the mean squared ℓ_2 distance between prediction probability vectors of k -NN neighbors, (iii) **k -NN conf absdiff** is the mean absolute difference in top-1 confidence between k -NN neighbors, and (iv) **k -NN margin absdiff** is the mean absolute difference in true-class log-probability margin between k -NN neighbors.

We show the results in Table 4 for a TBNN-LinEmb model for all three domain adaptation scenarios using the trained source-only and DAN models. We omit hard-label metrics from the sim-to-sim analysis because the dataset uses multi-proportion (soft) labels. Uncertainties (\pm) represent sample standard deviations across the 10 randomized trials described in Section 3.2. We tested for statistical significance using a two-sided Wilcoxon signed-rank test, testing the null hypothesis that there is no difference in diagnostic metric value between the two models. For the sim-to-real LaBr₃ scenario, we find that the DAN model wins in 9 out of 12 metrics, the source-only model in 1 out of 12, and 2 out of 12 considered statistically insignificant. We see similar results for the sim-to-real NaI(Tl) scenario (DAN wins 7, source-only wins 1, 4 statistically insignificant). Overall, we present statistical evidence that in the sim-to-real scenarios, UDA improves model performance in a range of calibration, separation, uncertainty, and input-space smoothness metrics.

4.5. Model Explainability

To gain insight into our models’ decision-making process, we used SHapley Additive exPlanations (SHAP) [16, 66] to compute per-region feature attributions. For a given gamma spectrum, SHAP produces an *explanation vector* of SHAP values by assigning an attribution to each spectral region, indicating how that region shifts the model predicted isotope probability relative to a baseline. The SHAP values are computed by repeatedly masking random regions of a spectrum, evaluating the model on the perturbed spectrum, and then averaging each region’s marginal contribution. In this context, we mask a region by replacing the counts in the selected bins with values obtained by log-linear interpolation between the region’s endpoints. Regions with large positive (negative) SHAP values increase (decrease) the predicted probability for a given isotope, while values near zero indicate little average effect. We find that, compared to the source-only model, the domain-adapted model is more likely to identify physically descriptive features of the true isotope rather than spurious peaks arising from contamination, background, or detector intrinsics. We include three such examples in Fig. 2, where we use a colorbar to overlay the computed SHAP values for the model’s predicted class on top of the experimental spectrum, comparing the source-only models to the domain-adapted models for different isotopes and detector types.

Table 4: Comparing the effects of UDA on a variety of diagnostic metrics (\uparrow higher is better, \downarrow lower is better). Source-only and UDA TBNN-LinEmb models are shown for all three domain adaptation scenarios. Entries for the best model are bolded when significant ($p < 0.01$). Overall, UDA provides improvements using a wide variety of metrics beyond classification accuracy in the sim-to-real scenarios.

(a) Scenario: sim-to-sim (HPGe).

Metric	Source-only	DAN	p -value	Dir.	Type
APE Score	0.653 \pm 0.004	0.667 \pm 0.004	0.002	\uparrow	Task Score
Negative log-likelihood [57]	3.499 \pm 0.051	3.180 \pm 0.019	0.002	\downarrow	Likelihood / Loss
Brier score [58]	0.056 \pm 0.003	0.057 \pm 0.002	0.322	\downarrow	Calibration
Mean Jacobian norm [62]	0.106 \pm 0.010	0.066 \pm 0.008	0.002	\downarrow	Sensitivity
k -NN prob ℓ_2 [63, 64]	0.200 \pm 0.010	0.233 \pm 0.006	0.002	\downarrow	Smoothness
k -NN conf absdiff [63, 64]	0.100 \pm 0.006	0.120 \pm 0.007	0.002	\downarrow	Smoothness

(b) Scenario: sim-to-real (LaBr₃)

Metric	Source-only	DAN	p -value	Dir.	Type
Accuracy	0.754 \pm 0.010	0.904 \pm 0.021	0.002	\uparrow	Accuracy
Negative log-likelihood [57]	2.840 \pm 0.317	0.393 \pm 0.125	0.002	\downarrow	Likelihood / Loss
Brier score [58]	0.455 \pm 0.037	0.147 \pm 0.031	0.002	\downarrow	Calibration
Expected calibration error [59]	0.218 \pm 0.025	0.044 \pm 0.014	0.002	\downarrow	Calibration
Prediction margin (mean) [60]	6.646 \pm 0.544	8.853 \pm 1.055	0.002	\uparrow	Separation / Margin
Prediction margin (p10) [60]	-13.543 \pm 1.765	0.217 \pm 1.116	0.002	\uparrow	Separation / Margin
AUROC (Entropy) [65]	0.902 \pm 0.036	0.940 \pm 0.015	0.004	\uparrow	Uncertainty
Mean Jacobian norm [62]	2.151 \pm 0.498	3.348 \pm 2.423	0.322	\downarrow	Sensitivity
k -NN TV hard [63, 64]	0.959 \pm 0.002	0.959 \pm 0.003	0.515	\downarrow	Boundary Complexity
k -NN prob ℓ_2 [63, 64]	1.880 \pm 0.026	1.839 \pm 0.023	0.004	\downarrow	Smoothness
k -NN conf absdiff [63, 64]	0.028 \pm 0.017	0.054 \pm 0.014	0.002	\downarrow	Smoothness
k -NN margin absdiff [63, 64]	7.666 \pm 0.426	4.890 \pm 0.649	0.002	\downarrow	Smoothness

(c) Scenario: sim-to-real (NaI(Tl))

Metric	Source-only	DAN	p -value	Dir.	Type
Accuracy	0.749 \pm 0.014	0.905 \pm 0.021	0.002	\uparrow	Accuracy
Negative log-likelihood [57]	2.175 \pm 0.228	0.418 \pm 0.120	0.002	\downarrow	Likelihood / Loss
Brier score [58]	0.452 \pm 0.023	0.154 \pm 0.037	0.002	\downarrow	Calibration
Expected calibration error [59]	0.217 \pm 0.013	0.061 \pm 0.022	0.002	\downarrow	Calibration
Prediction margin (mean) [60]	7.906 \pm 0.389	10.239 \pm 0.755	0.002	\uparrow	Separation / Margin
Prediction margin (p10) [60]	-9.823 \pm 1.128	0.286 \pm 1.021	0.002	\uparrow	Separation / Margin
AUROC (Entropy) [65]	0.921 \pm 0.011	0.923 \pm 0.023	0.846	\uparrow	Uncertainty
Mean Jacobian norm [62]	4.259 \pm 1.011	3.320 \pm 1.567	0.131	\downarrow	Sensitivity
k -NN TV hard [63, 64]	0.963 \pm 0.003	0.972 \pm 0.001	0.002	\downarrow	Boundary Complexity
k -NN prob ℓ_2 [63, 64]	1.880 \pm 0.016	1.876 \pm 0.024	1.000	\downarrow	Smoothness
k -NN conf absdiff [63, 64]	0.032 \pm 0.014	0.043 \pm 0.017	0.232	\downarrow	Smoothness
k -NN margin absdiff [63, 64]	7.840 \pm 0.600	5.902 \pm 0.560	0.002	\downarrow	Smoothness

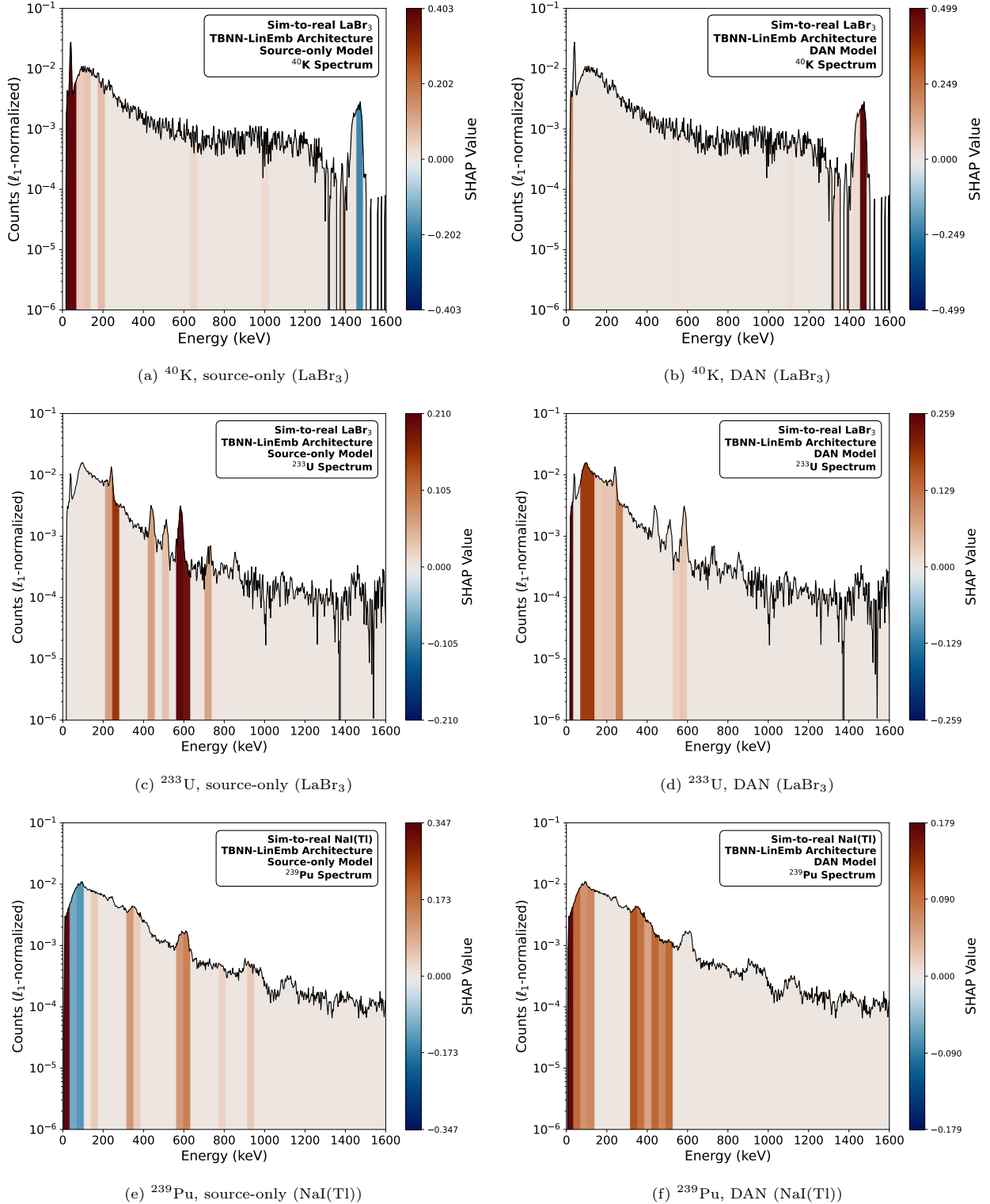


Figure 2: SHAP explanations comparing source-only (left panels) and DAN models (right panels) across three experimental example spectra. For ^{40}K (top row), the source-only model highlights the LaBr₃ detector’s intrinsic 32 keV X-ray peak, whereas the DAN model instead identifies the correct 1460 keV line. For ^{233}U (middle row), the source-only model relies primarily on peaks associated with visible ^{232}U -chain contamination, while the DAN model identifies the more subtle 93 keV feature of ^{233}U . For ^{239}Pu (bottom row), the source-only model predicts ^{124}Sb by emphasizing the 603 keV peak (likely due to trace contamination or activation-related background), whereas the DAN model highlights the characteristic ^{239}Pu peaks around 345, 375, and 413 keV.

5. Discussion

Section 4.1 highlights the underlying motivation for this study: simulated and experimental gamma spectra have a quantifiable gap in data distributions. From a physical standpoint, the sim-to-real gap arises from a range of confounding factors: imperfect detector response modeling, unpredictable backgrounds, environmental contributions, complex geometric effects, shielding, class imbalance, and so on. These effects distort spectra in a way that will inevitably degrade the performance of a machine learning model trained on simulations and tested on experimental data. Section 4.2 reveals that this domain gap can be partially overcome using UDA. Succinctly, UDA is able to target global feature distribution mismatch without imposing strong assumptions about the nature of the shift. Intuitively, the domain-adapted models have learned how to represent experimental data in a way that matches the patterns learned from simulations.

We remark that the magnitude of the improvement from UDA was substantially different between the sim-to-sim and sim-to-real domain adaptation scenarios. In sim-to-sim, we only observed a modest improvement to testing APE score. This may be due to substantial concept shift, but could also stem from the increased difficulty of 55-class multi-label proportion estimation. The sim-to-real scenario yielded a more significant improvement to testing accuracy, which was initially surprising due to the minimal qualitative improvement to feature alignment as seen in Fig. 1c–1f. We interpret this as evidence that the domain gap in the sim-to-real scenario does not manifest itself as poor 2D UMAP cluster alignment, but rather in the form of complex, high-dimensional feature incongruence which is relevant to the decision boundary.

Furthermore, we observe a performance discrepancy between different UDA methods. DAN and DANN appear to provide the most consistent improvements across a wide range of architectures, likely stemming from their simplicity and minimal assumptions regarding domain shift type. In contrast, augmentation-based methods such as Mean Teacher and SimCLR achieve less consistent gains, suggesting that Poisson resampling alone is insufficient to capture systematic distortions which contribute to the domain gap. This hypothesis is strengthened by the lack of apparent domain alignment shown in Figs. A.3g and A.3h. Interestingly, DeepCORAL’s impressive results were limited to the CNN backbone, suggesting covariance-based alignment effectively captures the hierarchical, spatially-structured features with strong local correlations produced by CNNs.

Finally, SHAP (Section 4.5) helps us understand and explain the decision making process of our models, providing further intuition behind the improvements from UDA. For instance, Fig. 2a reveals that the source-only model identifies the LaBr₃ detector’s intrinsic 32 keV Ba K-shell X-ray peak as salient, confusing it with the 40 keV X-rays emitted from electron capture on ¹⁵²Eu. On the contrary, Fig. 2b demonstrates that the DAN model correctly learns to ignore the 32 keV characteristic X-ray and instead focus on the 1460 keV peak from ⁴⁰K. As a result, the DAN model achieves a ⁴⁰K classification accuracy of 83%, compared to 17% from the source-only model. We make similar observations in Figs. 2c and 2e, where the source-only model focuses on miscellaneous peaks stemming from trace contamination, likely because these contaminants were not included in the source-domain simulations and thus the model did not learn to ignore them. On the contrary, we see in Figs. 2d and 2f that the domain-adapted model has learned to instead focus on features that are stable across simulation and experiment.

6. Conclusions

This study uses UDA to improve the performance of radioisotope identification models in scenarios where target-domain data is available but lacks ground-truth labels. We compared several different UDA methods

(ADDA, DAN, DANN, DeepCORAL, DeepJDOT, Mean Teacher, SimCLR) and architectural backbones (MLP, CNN, TBNN), finding that UDA provides a statistically significant improvement to testing scores in both sim-to-sim and sim-to-real scenarios. These improvements were more pronounced in the sim-to-real studies, where we found that DAN and DANN reliably yielded double digit improvements to testing accuracy across the MLP and TBNN model families. For instance, the DAN TBNN-LinEmb achieves a testing accuracy of 0.904 ± 0.022 on the experimental LaBr₃ dataset, compared to 0.754 ± 0.014 of the source-only model. The improvements in the sim-to-sim scenario were less pronounced but still statistically significant, validating the hypothesis that domain shift in sim-to-sim was more challenging to resolve using unsupervised feature alignment.

We support the conclusions of this study using a range of quantitative diagnostic metrics and qualitative explainability techniques. In addition to testing accuracy, DAN achieves improved likelihood, calibration, and margin compared to the source-only model on the sim-to-real LaBr₃ dataset. Furthermore, we have identified cases where the DAN model highlights salient spectral features instead of overfitting to spurious high-count, lower-energy peaks. Overall, we find that UDA is a practical tool for adapting synthetic-pretrained ML methods for radioisotope identification tasks in operational scenarios where unlabeled experimental datasets are available.

We identify several avenues for future work. First, it would be valuable to consider more challenging sim-to-real scenarios, including mixed sources and low-SNR datasets. Second, follow-on investigations should analyze the effect of dataset size on UDA effectiveness. Third, a more comprehensive SHAP analysis across all isotopes and shielding configurations, potentially summarized using a global SHAP statistic, would be desirable. Fourth, future research should consider additional sources of domain shift, including scenarios where certain isotope classes are missing from the target-domain dataset. Lastly, future work should investigate a *real-to-real* domain adaptation scenario in which data collected from one experiment is used in conjunction with a different but related task.

7. Data Availability

Datasets and model training code can be found at <https://github.com/pnnl/gamma-adapt/> for the sim-to-sim domain adaptation scenario. Due to data sensitivity, the code, data, and best models for the sim-to-real dataset are not available for public release.

8. Acknowledgements

This research was supported by the Laboratory Directed Research and Development Program at Pacific Northwest National Laboratory, a multiprogram national laboratory operated by Battelle for the U.S. Department of Energy under contract DE-AC05-76RLO1830. Peter Lalor is grateful for the support of the Linus Pauling Distinguished Postdoctoral Fellowship. The authors would like to acknowledge Tyler Morrow and Brian Archambault for their useful suggestions and feedback. The authors declare no conflict of interest.

9. Declaration of generative AI and AI-assisted technologies in the manuscript preparation process

During the preparation of this work the authors used generative AI tools in order to assist with language editing and formatting. After using this tool/service, the authors reviewed and edited the content as needed and take full responsibility for the content of the published article.

References

- [1] D. Breitenmoser, A. Stabilini, M. M. Kasprzak, S. Mayer, Quantitative mobile gamma-ray spectrometry through Bayesian inference (Jan. 2026). [arXiv:2512.18769](#), [doi:10.48550/arXiv.2512.18769](#).
- [2] P. R. Fernández, C. Svinth, A. Hagen, Improvement of Nuclide Detection through Graph Spectroscopic Analysis Framework and its Application to Nuclear Facility Upset Detection (Jun. 2025). [arXiv:2506.16522](#), [doi:10.48550/arXiv.2506.16522](#).
- [3] S. E. Labov, K. E. Nelson, C. M. Mattoon, N. J. McFerran, M. H. Pham, L. Her, J. S. Brzosko, S. Ray, D. Howarth, A. W. Dubrawski, Improving operational performance using machine learning analysis of Radiation Portal Monitor measurements, *Nuclear Instruments and Methods in Physics Research Section A: Accelerators, Spectrometers, Detectors and Associated Equipment* 1072 (2025) 170123. [doi:10.1016/j.nima.2024.170123](#).
- [4] P. Lalor, H. Adams, A. Hagen, Sim-to-real supervised domain adaptation for radioisotope identification, *Nuclear Instruments and Methods in Physics Research Section A: Accelerators, Spectrometers, Detectors and Associated Equipment* 1083 (2026) 171159. [doi:https://doi.org/10.1016/j.nima.2025.171159](#).
URL <https://www.sciencedirect.com/science/article/pii/S0168900225009611>
- [5] G. F. Knoll, *Radiation Detection and Measurement*, 4th Edition, Wiley, Hoboken, NJ, 2010.
- [6] M. A. Mariscotti, A method for automatic identification of peaks in the presence of background and its application to spectrum analysis, *Nuclear Instruments and Methods* 50 (2) (1967) 309–320. [doi:10.1016/0029-554X\(67\)90058-4](#).
- [7] Genie 2000 Operations Manual.
- [8] P. Viola, M. Jones, Rapid object detection using a boosted cascade of simple features, in: *Proceedings of the 2001 IEEE Computer Society Conference on Computer Vision and Pattern Recognition. CVPR 2001*, Vol. 1, 2001, pp. I–I. [doi:10.1109/CVPR.2001.990517](#).
- [9] Z. Zou, K. Chen, Z. Shi, Y. Guo, J. Ye, Object Detection in 20 Years: A Survey (Jan. 2023). [arXiv:1905.05055](#), [doi:10.48550/arXiv.1905.05055](#).
- [10] F. James, MINUIT: Function Minimization and Error Analysis Reference Manual, CERN Program Library Long Writeup D506, Conseil Européen pour la Recherche Nucléaire (CERN), Geneva (1994).
- [11] L. Reuter, G. D. Pietro, S. Stefkova, T. Ferber, V. Bertacchi, G. Casarosa, L. Corona, P. Ecker, A. Glazov, Y. Han, M. Laurenza, T. Lueck, L. Massaccesi, S. Mondal, B. Scavino, S. Spataro, C. Wessel, L. Zani, End-to-End Multi-Track Reconstruction using Graph Neural Networks at Belle II (Nov. 2024). [arXiv:2411.13596](#), [doi:10.48550/arXiv.2411.13596](#).
- [12] A. Krizhevsky, I. Sutskever, G. E. Hinton, ImageNet Classification with Deep Convolutional Neural Networks, in: *Advances in Neural Information Processing Systems*, Vol. 25, Curran Associates, Inc., 2012.
- [13] J. Hestness, S. Narang, N. Ardalani, G. Diamos, H. Jun, H. Kianinejad, M. M. A. Patwary, Y. Yang, Y. Zhou, Deep Learning Scaling is Predictable, Empirically (Dec. 2017). [arXiv:1712.00409](#), [doi:10.48550/arXiv.1712.00409](#).
- [14] I. Alabdulmohsin, B. Neyshabur, X. Zhai, Revisiting Neural Scaling Laws in Language and Vision (Nov. 2022). [arXiv:2209.06640](#), [doi:10.48550/arXiv.2209.06640](#).
- [15] J. M. Ghawaly, A. D. Nicholson, D. E. Archer, M. J. Willis, I. Garishvili, B. Longmire, A. J. Rowe, I. R. Stewart, M. T. Cook, Characterization of the autoencoder radiation anomaly detection (arad) model, *Engineering Applications of Artificial Intelligence* 111 (2022) 104761. [doi:10.1016/j.engappai.2022.](#)

104761.

URL <https://www.sciencedirect.com/science/article/pii/S0952197622000550>

- [16] M. S. Bandstra, J. C. Curtis, J. M. Ghawaly, Jr, A. C. Jones, T. H. Y. Joshi, Explaining machine-learning models for gamma-ray detection and identification, *PLOS ONE* 18 (6) (2023) 1–21. doi:10.1371/journal.pone.0286829.
URL <https://doi.org/10.1371/journal.pone.0286829>
- [17] K. J. Bilton, T. H. Y. Joshi, M. S. Bandstra, J. C. Curtis, D. Hellfeld, K. Vetter, Neural network approaches for mobile spectroscopic gamma-ray source detection, *Journal of Nuclear Engineering* 2 (2) (2021) 190–206. doi:10.3390/jne2020018.
URL <https://www.mdpi.com/2673-4362/2/2/18>
- [18] A. Farahani, S. Voghoei, K. Rasheed, H. R. Arabnia, A Brief Review of Domain Adaptation (Oct. 2020). arXiv:2010.03978, doi:10.48550/arXiv.2010.03978.
- [19] A. Vaswani, N. Shazeer, N. Parmar, J. Uszkoreit, L. Jones, A. N. Gomez, Ł. Kaiser, I. Polosukhin, Attention is all you need, in: *Advances in Neural Information Processing Systems*, Vol. 2017-Decem, Neural information processing systems foundation, 2017, pp. 5999–6009. arXiv:1706.03762.
- [20] T. B. Brown, B. Mann, N. Ryder, M. Subbiah, J. Kaplan, P. Dhariwal, A. Neelakantan, P. Shyam, G. Sastry, A. Askell, S. Agarwal, A. Herbert-Voss, G. Krueger, T. Henighan, R. Child, A. Ramesh, D. M. Ziegler, J. Wu, C. Winter, C. Hesse, M. Chen, E. Sigler, M. Litwin, S. Gray, B. Chess, J. Clark, C. Berner, S. McCandlish, A. Radford, I. Sutskever, D. Amodei, Language Models are Few-Shot Learners (Jul. 2020). arXiv:2005.14165, doi:10.48550/arXiv.2005.14165.
- [21] A. Radford, K. Narasimhan, T. Salimans, I. Sutskever, Improving Language Understanding by Generative Pre-Training.
- [22] A. Radford, J. Wu, R. Child, D. Luan, D. Amodei, I. Sutskever, Language Models are Unsupervised Multitask Learners.
- [23] J. Devlin, M.-W. Chang, K. Lee, K. Toutanova, BERT: Pre-training of Deep Bidirectional Transformers for Language Understanding (May 2019). arXiv:1810.04805, doi:10.48550/arXiv.1810.04805.
- [24] C. Ly, W. Frazier, A. Olsen, I. Schwerdt, L. W. McDonald, A. Hagen, Improving microstructures segmentation via pretraining with synthetic data, *Computational Materials Science* 249 (2025) 113639. doi:10.1016/j.commatsci.2024.113639.
- [25] A. Jain, A. Montanari, E. Sasoglu, Scaling laws for learning with real and surrogate data, *Advances in Neural Information Processing Systems* 37 (2024) 110246–110289.
- [26] J. G. Moreno-Torres, T. Raeder, R. Alaiz-Rodríguez, N. V. Chawla, F. Herrera, A unifying view on dataset shift in classification, *Pattern Recognition* 45 (1) (2012) 521–530. doi:<https://doi.org/10.1016/j.patcog.2011.06.019>.
URL <https://www.sciencedirect.com/science/article/pii/S0031320311002901>
- [27] J. Quiñero-Candela, M. Sugiyama, A. Schwaighofer, N. D. Lawrence (Eds.), *Dataset Shift in Machine Learning*, MIT Press, Cambridge, MA, 2009.
- [28] P. Olmos, J. Diaz, J. Perez, P. Gomez, V. Rodellar, P. Aguayo, A. Bru, G. Garcia-Belmonte, J. de Pablos, A new approach to automatic radiation spectrum analysis, *IEEE Transactions on Nuclear Science* 38 (4) (1991) 971–975. doi:10.1109/23.83860.
- [29] P. Olmos, J. Diaz, J. Perez, G. Garcia-Belmonte, P. Gomez, V. Rodellar, Application of neural network techniques in gamma spectroscopy, *Nuclear Instruments and Methods in Physics Research Section A: Accelerators, Spectrometers, Detectors and Associated Equipment* 312 (1) (1992) 167–173. doi:[https://doi.org/10.1016/0168-9002\(92\)90001-4](https://doi.org/10.1016/0168-9002(92)90001-4)

[//doi.org/10.1016/0168-9002\(92\)90148-W](https://doi.org/10.1016/0168-9002(92)90148-W).

URL <https://www.sciencedirect.com/science/article/pii/016890029290148W>

- [30] M. Kamuda, J. Zhao, K. Huff, A comparison of machine learning methods for automated gamma-ray spectroscopy, *Nuclear Instruments and Methods in Physics Research Section A: Accelerators, Spectrometers, Detectors and Associated Equipment* 954 (2020) 161385, symposium on Radiation Measurements and Applications XVII. doi:10.1016/j.nima.2018.10.063.
URL <https://www.sciencedirect.com/science/article/pii/S0168900218313779>
- [31] D. Liang, P. Gong, X. Tang, P. Wang, L. Gao, Z. Wang, R. Zhang, Rapid nuclide identification algorithm based on convolutional neural network, *Annals of Nuclear Energy* 133 (2019) 483–490. doi:10.1016/j.anucene.2019.05.051.
URL <https://www.sciencedirect.com/science/article/pii/S0306454919303044>
- [32] E. T. Moore, W. P. Ford, E. J. Hague, J. Turk, An application of cnns to time sequenced one dimensional data in radiation detection (2019). arXiv:1908.10887.
URL <https://arxiv.org/abs/1908.10887>
- [33] E. T. Moore, J. L. Turk, W. P. Ford, N. J. Hoteling, L. S. McLean, Transfer learning in automated gamma spectral identification (2020). arXiv:2003.10524.
URL <https://arxiv.org/abs/2003.10524>
- [34] G. Daniel, F. Ceraudo, O. Limousin, D. Maier, A. Meuris, Automatic and real-time identification of radionuclides in gamma-ray spectra: A new method based on convolutional neural network trained with synthetic data set, *IEEE Transactions on Nuclear Science* 67 (4) (2020) 644–653. doi:10.1109/TNS.2020.2969703.
- [35] N. Barradas, A. Vieira, M. Felizardo, M. Matos, Nuclide identification of radioactive sources from gamma spectra using artificial neural networks, *Radiation Physics and Chemistry* 232 (2025) 112692. doi:<https://doi.org/10.1016/j.radphyschem.2025.112692>.
URL <https://www.sciencedirect.com/science/article/pii/S0969806X25001847>
- [36] F. Li, C.-Y. Luo, Y.-Z. Wen, S. Lv, F. Cheng, G.-Q. Zeng, J.-F. Jiang, B.-H. Li, A nuclide identification method of γ spectrum and model building based on the transformer, *Nuclear Science and Techniques* 36 (1) (2024) 7. doi:10.1007/s41365-024-01564-5.
URL <https://doi.org/10.1007/s41365-024-01564-5>
- [37] A. Van Omen, T. Morrow, C. Scott, E. Leonard, Multilabel proportion prediction and out-of-distribution detection on gamma spectra of short-lived fission products, *Annals of Nuclear Energy* 208 (2024) 110777. doi:10.1016/j.anucene.2024.110777.
URL <https://www.sciencedirect.com/science/article/pii/S0306454924004407>
- [38] M. Abadi, A. Agarwal, P. Barham, E. Brevdo, Z. Chen, C. Citro, G. S. Corrado, A. Davis, J. Dean, M. Devin, S. Ghemawat, I. Goodfellow, A. Harp, G. Irving, M. Isard, Y. Jia, R. Jozefowicz, L. Kaiser, M. Kudlur, J. Levenberg, D. Mané, R. Monga, S. Moore, D. Murray, C. Olah, M. Schuster, J. Shlens, B. Steiner, I. Sutskever, K. Talwar, P. Tucker, V. Vanhoucke, V. Vasudevan, F. Viégas, O. Vinyals, P. Warden, M. Wattenberg, M. Wicke, Y. Yu, X. Zheng, TensorFlow: Large-scale machine learning on heterogeneous systems, software available from tensorflow.org (2015).
URL <https://www.tensorflow.org/>
- [39] E. Tzeng, J. Hoffman, K. Saenko, T. Darrell, Adversarial discriminative domain adaptation (2017). arXiv:1702.05464.
URL <https://arxiv.org/abs/1702.05464>

- [40] M. Long, Y. Cao, J. Wang, M. I. Jordan, Learning transferable features with deep adaptation networks (2015). [arXiv:1502.02791](https://arxiv.org/abs/1502.02791).
URL <https://arxiv.org/abs/1502.02791>
- [41] Y. Ganin, E. Ustinova, H. Ajakan, P. Germain, H. Larochelle, F. Laviolette, M. Marchand, V. Lempitsky, Domain-adversarial training of neural networks (2016). [arXiv:1505.07818](https://arxiv.org/abs/1505.07818).
URL <https://arxiv.org/abs/1505.07818>
- [42] B. Sun, K. Saenko, Deep coral: Correlation alignment for deep domain adaptation (2016). [arXiv:1607.01719](https://arxiv.org/abs/1607.01719).
URL <https://arxiv.org/abs/1607.01719>
- [43] B. B. Damodaran, B. Kellenberger, R. Flamary, D. Tuia, N. Courty, Deepjdot: Deep joint distribution optimal transport for unsupervised domain adaptation (2018). [arXiv:1803.10081](https://arxiv.org/abs/1803.10081).
URL <https://arxiv.org/abs/1803.10081>
- [44] A. Tarvainen, H. Valpola, Mean teachers are better role models: Weight-averaged consistency targets improve semi-supervised deep learning results (2018). [arXiv:1703.01780](https://arxiv.org/abs/1703.01780).
URL <https://arxiv.org/abs/1703.01780>
- [45] J. Stomps, P. Wilson, K. Dayman, M. Willis, J. Ghawaly, D. Archer, Data augmentations for nuclear feature extraction in semi-supervised contrastive machine learning, in: Proceedings of the INMM/ESARDA Joint Annual Meeting 2023, Institute of Nuclear Materials Management (INMM), Vienna, Austria, 2023.
URL <https://resources.inmm.org/annual-meeting-proceedings/data-augmentations-nuclear-feature-extraction>
- [46] T. Chen, S. Kornblith, M. Norouzi, G. Hinton, A simple framework for contrastive learning of visual representations (2020). [arXiv:2002.05709](https://arxiv.org/abs/2002.05709).
URL <https://arxiv.org/abs/2002.05709>
- [47] J. Allison, K. Amako, J. Apostolakis, P. Arce, M. Asai, T. Aso, E. Bagli, A. Bagulya, S. Banerjee, G. Barrand, B. Beck, A. Bogdanov, D. Brandt, J. Brown, H. Burkhardt, P. Canal, D. Cano-Ott, S. Chauvie, K. Cho, G. Cirrone, G. Cooperman, M. Cortés-Giraldo, G. Cosmo, G. Cuttone, G. Depaola, L. Desorgher, X. Dong, A. Dotti, V. Elvira, G. Folger, Z. Francis, A. Galoyan, L. Garnier, M. Gayer, K. Genser, V. Grichine, S. Guatelli, P. Guèye, P. Gumplinger, A. Howard, I. Hřivnáčová, S. Hwang, S. Incerti, A. Ivanchenko, V. Ivanchenko, F. Jones, S. Jun, P. Kaitaniemi, N. Karakatsanis, M. Karamitros, M. Kelsey, A. Kimura, T. Koi, H. Kurashige, A. Lechner, S. Lee, F. Longo, M. Maire, D. Mancusi, A. Mantero, E. Mendoza, B. Morgan, K. Murakami, T. Nikitina, L. Pandola, P. Paprocki, J. Perl, I. Petrović, M. Pia, W. Pokorski, J. Quesada, M. Raine, M. Reis, A. Ribon, A. Ristić Fira, F. Romano, G. Russo, G. Santin, T. Sasaki, D. Sawkey, J. Shin, I. Strakovsky, A. Taborda, S. Tanaka, B. Tomé, T. Toshito, H. Tran, P. Truscott, L. Urban, V. Uzhinsky, J. Verbeke, M. Verderi, B. Wendt, H. Wenzel, D. Wright, D. Wright, T. Yamashita, J. Yarba, H. Yoshida, Recent developments in geant4, Nuclear Instruments and Methods in Physics Research Section A: Accelerators, Spectrometers, Detectors and Associated Equipment 835 (2016) 186–225. doi:10.1016/j.nima.2016.06.125.
URL <https://www.sciencedirect.com/science/article/pii/S0168900216306957>
- [48] B. Archambault, B. Pierson, B. Loer, G4ares-geant4 advanced radio-emission simulation framework, available from <https://gitlab.pnnl.gov/ares/g4ares> [accessed November 20, 2024] (2023).
- [49] B. D. Pierson, B. C. Archambault, L. R. Greenwood, M. M. Haney, M. G. Cantaloub, A. R. Hagen, S. M. Herman, N. E. Uhnak, J. M. Bowen, J. H. Estrada, Alpha/beta-gated gamma–gamma spectroscopy of mixed fission products for trace analysis, Journal of Radioanalytical and Nuclear Chemistry 331 (12)

- (2022) 5453–5467. doi:10.1007/s10967-022-08606-5.
 URL <https://doi.org/10.1007/s10967-022-08606-5>
- [50] T. Morrow, N. Price, T. McGuire, Pyriid v.2.0.0, [Computer Software] (apr 2021). doi:10.11578/dc.20221017.2.
 URL <https://doi.org/10.11578/dc.20221017.2>
- [51] S. M. Horne, G. G. Thoreson, L. A. Theisen, D. J. Mitchell, L. Harding, W. A. Amai, Gadras-drf 18.6 user’s manual (5 2016). doi:10.2172/1431293.
 URL <https://www.osti.gov/biblio/1431293>
- [52] T. Akiba, S. Sano, T. Yanase, T. Ohta, M. Koyama, Optuna: A next-generation hyperparameter optimization framework, in: Proceedings of the 25th ACM SIGKDD International Conference on Knowledge Discovery & Data Mining, KDD ’19, Association for Computing Machinery, New York, NY, USA, 2019, p. 2623–2631. doi:10.1145/3292500.3330701.
 URL <https://doi.org/10.1145/3292500.3330701>
- [53] S. Ben-David, J. Blitzer, K. Crammer, A. Kulesza, F. Pereira, J. Vaughan, A theory of learning from different domains, Machine Learning 79 (2010) 151–175. doi:10.1007/s10994-009-5152-4.
- [54] A. Gretton, K. M. Borgwardt, M. J. Rasch, B. Schölkopf, A. Smola, A kernel two-sample test, J. Mach. Learn. Res. 13 (null) (2012) 723–773.
- [55] G. Peyré, M. Cuturi, Computational optimal transport, Found. Trends Mach. Learn. 11 (5–6) (2019) 355–607. doi:10.1561/22000000073.
 URL <https://doi.org/10.1561/22000000073>
- [56] L. McInnes, J. Healy, J. Melville, Umap: Uniform manifold approximation and projection for dimension reduction (2020). arXiv:1802.03426.
 URL <https://arxiv.org/abs/1802.03426>
- [57] K. P. Murphy, Machine learning: a probabilistic perspective, MIT press, 2012.
- [58] W. B. Glenn, et al., Verification of forecasts expressed in terms of probability, Monthly weather review 78 (1) (1950) 1–3.
- [59] C. Guo, G. Pleiss, Y. Sun, K. Q. Weinberger, On calibration of modern neural networks, in: International conference on machine learning, PMLR, 2017, pp. 1321–1330.
- [60] P. Bartlett, Y. Freund, W. S. Lee, R. E. Schapire, Boosting the margin: A new explanation for the effectiveness of voting methods, The annals of statistics 26 (5) (1998) 1651–1686.
- [61] D. Hendrycks, K. Gimpel, A baseline for detecting misclassified and out-of-distribution examples in neural networks (2018). arXiv:1610.02136.
 URL <https://arxiv.org/abs/1610.02136>
- [62] I. J. Goodfellow, J. Shlens, C. Szegedy, Explaining and harnessing adversarial examples, arXiv preprint arXiv:1412.6572 (2014).
- [63] M. Belkin, P. Niyogi, V. Sindhwani, Manifold regularization: A geometric framework for learning from labeled and unlabeled examples, Journal of Machine Learning Research 7 (85) (2006) 2399–2434.
 URL <http://jmlr.org/papers/v7/belkin06a.html>
- [64] X. Zhu, Z. Ghahramani, J. D. Lafferty, Semi-supervised learning using gaussian fields and harmonic functions, in: Proceedings of the 20th International conference on Machine learning (ICML-03), 2003, pp. 912–919.
- [65] C. E. Shannon, A mathematical theory of communication, The Bell system technical journal 27 (3) (1948) 379–423.

- [66] S. M. Lundberg, S.-I. Lee, A unified approach to interpreting model predictions, Curran Associates, Inc., 2017.
URL <http://papers.nips.cc/paper/7062-a-unified-approach-to-interpreting-model-predictions.pdf>
- [67] J. Bergstra, R. Bardenet, Y. Bengio, B. Kégl, Algorithms for hyper-parameter optimization, in: Advances in Neural Information Processing Systems 24, 2011, pp. 2546–2554.

Appendix A. Supplementary Materials

Appendix A.1. Hyperparameter optimization

Throughout the following tables, search spaces are annotated as follows: $[a, b]$ denotes continuous uniform sampling; $[a, b]_{\log}$ denotes continuous log-uniform sampling; $\{a, \dots, b\}$ denotes uniform sampling over consecutive integers; $[a, b]_{2^k}$ denotes uniform sampling over powers of two within the interval; and an explicitly listed finite set such as $\{3, 5, 7, 9\}$ indicates uniform sampling over its elements. All hyperparameter searches use the Tree-structured Parzen Estimator (TPE) sampler [67] implemented in Optuna [52]. We observe that some of the optimized hyperparameters in Tables A.5–A.13 fall at or near the boundary of their search space. The ranges reported here reflect the final iteration of several rounds of search-space refinement and note that hyperparameters which most strongly affect results (learning rate, UDA tradeoff parameter) are interior to the search space in the vast majority of configurations.

Table A.5: Source-only architecture hyperparameter optimization summary for MLP, CNN, TBNN (Li *et al.*), TBNN-LinEmb, and TBNN-NonlinEmb architectures. The table details the search spaces and best-performing hyperparameter values obtained via TPE Bayesian optimization using the source dataset from the sim-to-sim scenario. The best-performing hyperparameters are used for all models across different scenarios in this study. See the search space notation paragraph above for interval and sampling conventions.

Architecture	Parameter	Search Space	Best run
MLP	Num Dense Layers	$\{1, \dots, 4\}$	2
	Dense1 Hidden Units	$[512, 8192]_{2^k}$	8192
	Dense2 Hidden Units	$[256, 4096]_{2^k}$	4096
CNN	Num Convolutional Layers	$\{1, 2\}$	1
	Conv Filters	$[16, 256]_{2^k}$	16
	Conv Kernel Size	$\{3, 5, 7, 9\}$	5
	Num Dense Layers	$\{1, 2\}$	2
	Dense1 Hidden Units	$[512, 8192]_{2^k}$	4096
	Dense2 Hidden Units	$[256, 4096]_{2^k}$	2048
TBNN (Li <i>et al.</i>)	Num Attention Blocks	$\{1, \dots, 8\}$	4
	Num Heads	$[1, 8]_{2^k}$	4
	FF Dimension	$[64, 8192]_{2^k}$	2048
TBNN-LinEmb	Embedding Dimension	$[8, 1024]_{2^k}$	256
	Num Attention Blocks	$\{1, \dots, 5\}$	5
	Num Heads	$[1, 8]_{2^k}$	2
	FF Dimension	$[16, 16384]_{2^k}$	512
	Patch Size	$[16, 64]_{2^k}$	64
TBNN-NonLinEmb	Embedder Hidden Units	$[8, 2048]_{2^k}$	512
	Embedding Dimension	$[8, 1024]_{2^k}$	512
	Num Attention Blocks	$\{1, \dots, 5\}$	3
	Num Heads	$[1, 8]_{2^k}$	4
	FF Dimension	$[16, 16384]_{2^k}$	1024
	Patch Size	$[16, 64]_{2^k}$	64

Table A.6: Source-only training hyperparameter optimization summary for MLP, CNN, TBNN (Li *et al.*), TBNN-LinEmb, and TBNN-NonlinEmb architectures. The table details the search spaces and best-performing hyperparameter values obtained via TPE Bayesian optimization using the source dataset. See the search space notation paragraph for interval and sampling conventions.

Architecture	Parameter	Search Space	Best run		
			sim-to-sim HPGe	sim-to-real LaBr ₃	sim-to-real NaI(Tl)
MLP	Learning rate	$[10^{-5}, 2 \times 10^{-3}]_{\log}$	4.60e-5	1.80e-3	1.32e-3
	Batch size	$[32, 512]_{2^k}$	256	512	256
	Weight decay	$[10^{-7}, 10^{-3}]_{\log}$	1.54e-5	1.96e-6	1.21e-4
	Dropout	$[0.0, 0.4]$	0.230	0.394	0.224
CNN	Learning rate	$[10^{-5}, 2 \times 10^{-3}]_{\log}$	4.17e-5	1.07e-5	2.94e-4
	Batch size	$[32, 512]_{2^k}$	256	512	512
	Weight decay	$[10^{-7}, 10^{-3}]_{\log}$	5.77e-5	6.21e-4	1.25e-4
	Dropout	$[0.0, 0.4]$	0.205	0.220	0.272
TBNN (Li <i>et al.</i>)	Learning rate	$[10^{-5}, 2 \times 10^{-3}]_{\log}$	1.65e-3	1.28e-3	2.99e-4
	Batch size	$[32, 512]_{2^k}$	512	512	256
	Weight decay	$[10^{-7}, 10^{-3}]_{\log}$	9.06e-6	2.66e-5	5.39e-5
	Dropout	$[0.0, 0.1]$	3.31e-5	0.0349	0.0623
TBNN-LinEmb	Learning rate	$[10^{-5}, 2 \times 10^{-3}]_{\log}$	2.75e-4	1.01e-4	1.54e-4
	Batch size	$[32, 512]_{2^k}$	256	512	512
	Weight decay	$[10^{-7}, 10^{-3}]_{\log}$	1.23e-7	2.56e-6	8.89e-7
	Dropout	$[0.0, 0.1]$	2.90e-3	0.0413	0.0737
TBNN-NonLinEmb	Learning rate	$[10^{-5}, 2 \times 10^{-3}]_{\log}$	1.94e-4	2.27e-5	1.32e-4
	Batch size	$[32, 512]_{2^k}$	256	256	512
	Weight decay	$[10^{-7}, 10^{-3}]_{\log}$	2.47e-7	6.49e-4	3.39e-4
	Dropout	$[0.0, 0.1]$	3.24e-4	0.0479	0.0947

Table A.7: ADDA hyperparameter optimization summary for MLP, CNN, TBNN (Li *et al.*), TBNN-LinEmb, and TBNN-NonlinEmb architectures. The table details the search spaces and best-performing hyperparameter values obtained via TPE Bayesian optimization. See the search space notation paragraph for interval and sampling conventions.

Architecture	Parameter	Search Space	Best run		
			sim-to-sim HPGe	sim-to-real LaBr ₃	sim-to-real NaI(Tl)
MLP	FE learning rate [†]	$[10^{-8}, 10^{-2}]_{\log}$	5.87e-7	1.67e-4	2.18e-4
	DD learning rate [†]	$[10^{-8}, 10^{-2}]_{\log}$	9.29e-6	3.87e-6	5.03e-6
	Batch size	$[64, 512]_{2^k}$	128	128	64
	Weight decay	$[10^{-7}, 10^{-3}]_{\log}$	6.89e-6	2.35e-6	8.33e-4
	Dropout	$[0.0, 0.4]$	0.384	0.282	0.156
	Num discriminator layers	$\{1, 2\}$	2	2	1
	Discriminator dense1 units	$[512, 4096]_{2^k}$	2048	4096	4096
	Discriminator dense2 units	$[256, 2048]_{2^k}$	1024	2048	N/A
CNN	FE learning rate [†]	$[10^{-8}, 10^{-2}]_{\log}$	4.01e-7	6.25e-7	3.99e-5
	DD learning rate [†]	$[10^{-8}, 10^{-2}]_{\log}$	4.75e-6	7.67e-6	5.78e-4
	Batch size	$[64, 512]_{2^k}$	128	256	256
	Weight decay	$[10^{-7}, 10^{-3}]_{\log}$	6.51e-4	4.36e-6	4.13e-6
	Dropout	$[0.0, 0.4]$	0.394	0.270	0.114
	Num discriminator layers	$\{1, 2\}$	2	2	2
	Discriminator dense1 units	$[512, 4096]_{2^k}$	1024	512	512
	Discriminator dense2 units	$[256, 2048]_{2^k}$	512	256	256
TBNN (Li <i>et al.</i>)	FE learning rate [†]	$[10^{-8}, 10^{-2}]_{\log}$	3.09e-5	5.28e-5	2.81e-5
	DD learning rate [†]	$[10^{-8}, 10^{-2}]_{\log}$	2.10e-4	8.43e-6	2.76e-6
	Batch size	$[64, 512]_{2^k}$	64	128	512
	Weight decay	$[10^{-7}, 10^{-3}]_{\log}$	2.20e-6	9.73e-4	4.95e-7
	Dropout	$[0.0, 0.4]$	6.30e-3	0.0561	0.103
	Num discriminator layers	$\{1, 2\}$	1	1	1
	Discriminator dense1 units	$[512, 4096]_{2^k}$	512	1024	4096
	Discriminator dense2 units	$[256, 2048]_{2^k}$	N/A	N/A	N/A
TBNN-LinEmb	FE learning rate [†]	$[10^{-8}, 10^{-2}]_{\log}$	8.53e-6	3.24e-6	7.33e-6
	DD learning rate [†]	$[10^{-8}, 10^{-2}]_{\log}$	4.21e-4	9.38e-6	8.65e-6
	Batch size	$[64, 512]_{2^k}$	256	128	64
	Weight decay	$[10^{-7}, 10^{-3}]_{\log}$	4.56e-6	4.88e-4	1.57e-7
	Dropout	$[0.0, 0.4]$	0.114	0.221	0.203
	Num discriminator layers	$\{1, 2\}$	1	2	2
	Discriminator dense1 units	$[512, 4096]_{2^k}$	4096	1024	4096
	Discriminator dense2 units	$[256, 2048]_{2^k}$	N/A	512	2048
TBNN-NonLinEmb	FE learning rate [†]	$[10^{-8}, 10^{-2}]_{\log}$	1.34e-6	5.15e-6	4.70e-6
	DD learning rate [†]	$[10^{-8}, 10^{-2}]_{\log}$	9.51e-5	1.95e-5	2.23e-6
	Batch size	$[64, 512]_{2^k}$	64	64	512
	Weight decay	$[10^{-7}, 10^{-3}]_{\log}$	4.65e-6	2.88e-7	1.36e-5
	Dropout	$[0.0, 0.4]$	8.69e-3	0.196	0.0285
	Num discriminator layers	$\{1, 2\}$	2	2	1
	Discriminator dense1 units	$[512, 4096]_{2^k}$	4096	4096	2048
	Discriminator dense2 units	$[256, 2048]_{2^k}$	2048	2048	N/A

[†]The FE and DD learning rates are jointly parameterized as $\ell_{\text{FE}} = \ell/\sqrt{r}$ and $\ell_{\text{DD}} = \ell\sqrt{r}$, where $\ell \in [10^{-7}, 10^{-3}]_{\log}$ is a shared base learning rate and $r \in [10^{-2}, 10^2]_{\log}$ is a ratio parameter. The intervals shown are the effective ranges.

Table A.8: Same as Table A.7, but using DAN.

Architecture	Parameter	Search Space	Best run		
			sim-to-sim HPGe	sim-to-real LaBr ₃	sim-to-real NaI(Tl)
MLP	Learning rate	$[10^{-7}, 10^{-3}]_{\log}$	5.80e-6	9.72e-4	6.84e-4
	Batch size	$[64, 512]_{2^k}$	256	256	128
	Weight decay	$[10^{-7}, 10^{-3}]_{\log}$	1.92e-5	8.15e-5	6.24e-6
	Dropout	[0.0, 0.4]	0.0278	1.10e-3	3.71e-3
	Tradeoff parameter	$[10^{-1}, 10^4]_{\log}$	7397	871	1100
	RBF bandwidth	$[10^{-1}, 10^2]_{\log}$	58.3	6.22	16.9
	Number of kernels	{3, 5, 7, ..., 15}	9	15	11
CNN	Learning rate	$[10^{-7}, 10^{-3}]_{\log}$	8.73e-4	2.17e-4	8.04e-4
	Batch size	$[64, 512]_{2^k}$	64	512	256
	Weight decay	$[10^{-7}, 10^{-3}]_{\log}$	1.85e-4	1.42e-6	4.27e-7
	Dropout	[0.0, 0.4]	0.283	0.396	0.381
	Tradeoff parameter	$[10^{-1}, 10^4]_{\log}$	34.4	11.0	45.8
	RBF bandwidth	$[10^{-1}, 10^2]_{\log}$	9.32	87.0	41.7
	Number of kernels	{3, 5, 7, ..., 15}	5	13	13
TBNN (Li <i>et al.</i>)	Learning rate	$[10^{-7}, 10^{-3}]_{\log}$	1.59e-4	7.47e-4	7.74e-4
	Batch size	$[64, 512]_{2^k}$	512	64	256
	Weight decay	$[10^{-7}, 10^{-3}]_{\log}$	7.01e-5	2.68e-5	3.30e-6
	Dropout	[0.0, 0.4]	0.0819	0.0198	0.213
	Tradeoff parameter	$[10^{-1}, 10^4]_{\log}$	247	286	159
	RBF bandwidth	$[10^{-1}, 10^2]_{\log}$	2.56	32.1	26.3
	Number of kernels	{3, 5, 7, ..., 15}	7	13	15
TBNN-LinEmb	Learning rate	$[10^{-7}, 10^{-3}]_{\log}$	2.52e-4	3.92e-4	4.08e-4
	Batch size	$[64, 512]_{2^k}$	256	512	256
	Weight decay	$[10^{-7}, 10^{-3}]_{\log}$	7.57e-4	5.19e-7	1.38e-5
	Dropout	[0.0, 0.4]	0.125	0.165	0.272
	Tradeoff parameter	$[10^{-1}, 10^4]_{\log}$	4.31	381	185
	RBF bandwidth	$[10^{-1}, 10^2]_{\log}$	3.89	1.91	0.844
	Number of kernels	{3, 5, 7, ..., 15}	7	9	15
TBNN-NonLinEmb	Learning rate	$[10^{-7}, 10^{-3}]_{\log}$	5.19e-5	4.44e-4	4.70e-4
	Batch size	$[64, 512]_{2^k}$	512	512	512
	Weight decay	$[10^{-7}, 10^{-3}]_{\log}$	3.46e-5	9.19e-4	7.75e-5
	Dropout	[0.0, 0.4]	0.179	0.337	0.0733
	Tradeoff parameter	$[10^{-1}, 10^4]_{\log}$	54.9	440	168
	RBF bandwidth	$[10^{-1}, 10^2]_{\log}$	9.58	26.9	42.1
	Number of kernels	{3, 5, 7, ..., 15}	7	3	11

Table A.9: Same as Table A.7, but using DANN.

Architecture	Parameter	Search Space	Best run		
			sim-to-sim HPGe	sim-to-real LaBr ₃	sim-to-real NaI(Tl)
MLP	FE learning rate [†]	$[10^{-8}, 10^{-2}]_{\log}$	1.31e-6	1.05e-3	3.69e-4
	DD learning rate [†]	$[10^{-8}, 10^{-2}]_{\log}$	1.06e-5	1.52e-4	1.17e-4
	Batch size	$[64, 512]_{2^k}$	256	512	512
	Weight decay	$[10^{-7}, 10^{-3}]_{\log}$	1.26e-7	2.06e-4	1.12e-6
	Dropout	[0.0, 0.4]	0.0588	0.046	8.29e-3
	Num GRL layers	{1, 2}	1	2	2
	GRL dense1 units	$[64, 2048]_{2^k}$	1024	2048	64
	GRL dense2 units	$[32, 1024]_{2^k}$	N/A	1024	32
	GRL κ	[0.0, 1.0]	0.643	0.634	0.777
CNN	FE learning rate [†]	$[10^{-8}, 10^{-2}]_{\log}$	1.79e-3	1.24e-5	4.62e-5
	DD learning rate [†]	$[10^{-8}, 10^{-2}]_{\log}$	1.83e-4	4.29e-5	4.30e-4
	Batch size	$[64, 512]_{2^k}$	64	512	256
	Weight decay	$[10^{-7}, 10^{-3}]_{\log}$	8.55e-7	4.61e-4	1.06e-5
	Dropout	[0.0, 0.4]	0.386	9.40e-3	0.223
	Num GRL layers	{1, 2}	2	2	1
	GRL dense1 units	$[64, 2048]_{2^k}$	2048	2048	64
	GRL dense2 units	$[32, 1024]_{2^k}$	1024	1024	N/A
	GRL κ	[0.0, 1.0]	0.372	0.665	0.491
TBNN (Li <i>et al.</i>)	FE learning rate [†]	$[10^{-8}, 10^{-2}]_{\log}$	4.24e-5	1.27e-3	2.21e-3
	DD learning rate [†]	$[10^{-8}, 10^{-2}]_{\log}$	7.52e-5	3.89e-4	4.52e-4
	Batch size	$[64, 512]_{2^k}$	64	128	512
	Weight decay	$[10^{-7}, 10^{-3}]_{\log}$	2.93e-6	1.25e-5	2.41e-6
	Dropout	[0.0, 0.4]	0.0283	0.0215	0.328
	Num GRL layers	{1, 2}	1	2	2
	GRL dense1 units	$[64, 2048]_{2^k}$	128	512	256
	GRL dense2 units	$[32, 1024]_{2^k}$	N/A	256	128
	GRL κ	[0.0, 1.0]	0.573	0.89	0.117
TBNN-LinEmb	FE learning rate [†]	$[10^{-8}, 10^{-2}]_{\log}$	4.81e-5	1.01e-4	2.31e-4
	DD learning rate [†]	$[10^{-8}, 10^{-2}]_{\log}$	4.41e-5	2.80e-4	1.62e-3
	Batch size	$[64, 512]_{2^k}$	512	256	256
	Weight decay	$[10^{-7}, 10^{-3}]_{\log}$	1.99e-5	1.29e-4	5.97e-7
	Dropout	[0.0, 0.4]	0.139	0.0126	0.0986
	Num GRL layers	{1, 2}	2	2	2
	GRL dense1 units	$[64, 2048]_{2^k}$	1024	2048	512
	GRL dense2 units	$[32, 1024]_{2^k}$	512	1024	256
	GRL κ	[0.0, 1.0]	0.0676	0.665	0.813
TBNN-NonLinEmb	FE learning rate [†]	$[10^{-8}, 10^{-2}]_{\log}$	5.41e-5	5.21e-5	3.26e-4
	DD learning rate [†]	$[10^{-8}, 10^{-2}]_{\log}$	2.76e-5	2.37e-4	8.01e-4
	Batch size	$[64, 512]_{2^k}$	512	64	512
	Weight decay	$[10^{-7}, 10^{-3}]_{\log}$	1.54e-7	2.72e-5	1.18e-4
	Dropout	[0.0, 0.4]	0.193	0.162	0.123
	Num GRL layers	{1, 2}	2	2	2
	GRL dense1 units	$[64, 2048]_{2^k}$	1024	1024	2048
	GRL dense2 units	$[32, 1024]_{2^k}$	512	512	1024
	GRL κ	[0.0, 1.0]	0.207	0.456	0.718

[†]The FE and DD learning rates are jointly parameterized as $\ell_{\text{FE}} = \ell/\sqrt{r}$ and $\ell_{\text{DD}} = \ell\sqrt{r}$, where $\ell \in [10^{-7}, 10^{-3}]_{\log}$ is a shared base learning rate and $r \in [10^{-1}, 10^1]_{\log}$ is a ratio parameter. The intervals shown are the effective ranges.

Table A.10: Same as Table A.7, but using DeepCORAL.

Architecture	Parameter	Search Space	Best run		
			sim-to-sim HPGe	sim-to-real LaBr ₃	sim-to-real NaI(Tl)
MLP	Learning rate	$[10^{-7}, 10^{-3}]_{\log}$	1.34e-4	8.95e-4	9.41e-4
	Batch size	$[64, 512]_{2^k}$	512	512	128
	Weight decay	$[10^{-7}, 10^{-3}]_{\log}$	1.37e-6	1.19e-6	6.11e-7
	Dropout	[0.0, 0.4]	0.297	8.24e-3	0.0839
	Tradeoff parameter	$[10^{-1}, 10^{10}]_{\log}$	7.13e4	1.20e9	5.77e7
CNN	Learning rate	$[10^{-7}, 10^{-3}]_{\log}$	5.12e-4	2.97e-5	1.50e-5
	Batch size	$[64, 512]_{2^k}$	512	512	512
	Weight decay	$[10^{-7}, 10^{-3}]_{\log}$	2.21e-7	1.38e-7	1.90e-6
	Dropout	[0.0, 0.4]	0.036	5.71e-3	8.23e-3
	Tradeoff parameter	$[10^{-1}, 10^{10}]_{\log}$	2.82e5	1273	10.8
TBNN (Li <i>et al.</i>)	Learning rate	$[10^{-7}, 10^{-3}]_{\log}$	6.08e-4	7.82e-4	9.98e-4
	Batch size	$[64, 512]_{2^k}$	256	128	128
	Weight decay	$[10^{-7}, 10^{-3}]_{\log}$	5.70e-5	4.02e-4	1.83e-7
	Dropout	[0.0, 0.4]	5.46e-3	0.289	0.119
	Tradeoff parameter	$[10^{-1}, 10^{10}]_{\log}$	9.96e6	1.16e5	4.39e3
TBNN-LinEmb	Learning rate	$[10^{-7}, 10^{-3}]_{\log}$	3.69e-4	7.16e-4	4.75e-4
	Batch size	$[64, 512]_{2^k}$	512	512	512
	Weight decay	$[10^{-7}, 10^{-3}]_{\log}$	3.11e-4	1.21e-7	4.10e-6
	Dropout	[0.0, 0.4]	0.0566	0.228	0.0166
	Tradeoff parameter	$[10^{-1}, 10^{10}]_{\log}$	1.55e4	3.31e3	863
TBNN-NonLinEmb	Learning rate	$[10^{-7}, 10^{-3}]_{\log}$	1.24e-4	8.16e-4	5.21e-4
	Batch size	$[64, 512]_{2^k}$	512	512	512
	Weight decay	$[10^{-7}, 10^{-3}]_{\log}$	7.84e-7	9.77e-6	2.31e-5
	Dropout	[0.0, 0.4]	0.131	0.0632	0.221
	Tradeoff parameter	$[10^{-1}, 10^{10}]_{\log}$	1.85e4	3.78e3	3.65e3

Table A.11: Same as Table A.7, but using DeepJDOT.

Architecture	Parameter	Search Space	Best run		
			sim-to-sim HPGe	sim-to-real LaBr ₃	sim-to-real NaI(Tl)
MLP	Learning rate	$[10^{-7}, 10^{-3}]_{\log}$	9.25e-4	7.15e-4	7.24e-4
	Batch size	$[64, 512]_{2^k}$	512	512	256
	Weight decay	$[10^{-7}, 10^{-3}]_{\log}$	8.33e-6	5.23e-6	9.17e-4
	Dropout	[0.0, 0.4]	0.207	0.177	0.216
	Tradeoff parameter	$[10^{-2}, 10^2]_{\log}$	3.60	0.0204	0.0107
	Sinkhorn regularization	$[10^{-2}, 10^1]_{\log}$	8.47	4.36	7.57
	Sinkhorn iterations	{5, ..., 30}	11	24	17
	JDOT α	$[10^{-2}, 10^1]_{\log}$	0.397	0.205	1.14
	JDOT β	[0.0, 2.0]	1.36	0.222	1.41
CNN	Learning rate	$[10^{-7}, 10^{-3}]_{\log}$	7.18e-4	1.33e-6	9.03e-4
	Batch size	$[64, 512]_{2^k}$	64	512	128
	Weight decay	$[10^{-7}, 10^{-3}]_{\log}$	8.69e-4	1.02e-4	7.92e-7
	Dropout	[0.0, 0.4]	0.383	0.100	0.139
	Tradeoff parameter	$[10^{-2}, 10^2]_{\log}$	0.0754	2.24	1.31
	Sinkhorn regularization	$[10^{-2}, 10^1]_{\log}$	0.0364	1.85	0.0446
	Sinkhorn iterations	{5, ..., 30}	5	17	19
	JDOT α	$[10^{-2}, 10^1]_{\log}$	1.005	0.0167	0.0127
	JDOT β	[0.0, 2.0]	0.499	1.31	1.16
TBNN (Li <i>et al.</i>)	Learning rate	$[10^{-7}, 10^{-3}]_{\log}$	8.97e-5	2.25e-4	8.75e-4
	Batch size	$[64, 512]_{2^k}$	512	128	128
	Weight decay	$[10^{-7}, 10^{-3}]_{\log}$	3.57e-7	4.17e-5	1.56e-5
	Dropout	[0.0, 0.4]	0.0817	0.106	0.111
	Tradeoff parameter	$[10^{-2}, 10^2]_{\log}$	19.1	5.06	0.730
	Sinkhorn regularization	$[10^{-2}, 10^1]_{\log}$	0.0436	0.242	0.0132
	Sinkhorn iterations	{5, ..., 30}	7	19	5
	JDOT α	$[10^{-2}, 10^1]_{\log}$	0.0569	0.0126	0.0549
	JDOT β	[0.0, 2.0]	1.21	1.12	0.413
TBNN-LinEmb	Learning rate	$[10^{-7}, 10^{-3}]_{\log}$	2.81e-5	3.33e-5	1.94e-4
	Batch size	$[64, 512]_{2^k}$	64	64	128
	Weight decay	$[10^{-7}, 10^{-3}]_{\log}$	1.24e-6	7.67e-5	4.45e-4
	Dropout	[0.0, 0.4]	0.190	0.231	0.376
	Tradeoff parameter	$[10^{-2}, 10^2]_{\log}$	0.343	68.9	0.0533
	Sinkhorn regularization	$[10^{-2}, 10^1]_{\log}$	0.753	0.707	2.11
	Sinkhorn iterations	{5, ..., 30}	19	28	6
	JDOT α	$[10^{-2}, 10^1]_{\log}$	4.57	0.0119	0.239
	JDOT β	[0.0, 2.0]	0.532	1.01	1.89
TBNN-NonLinEmb	Learning rate	$[10^{-7}, 10^{-3}]_{\log}$	7.54e-4	3.17e-6	1.52e-4
	Batch size	$[64, 512]_{2^k}$	64	64	256
	Weight decay	$[10^{-7}, 10^{-3}]_{\log}$	5.23e-7	6.04e-5	1.80e-5
	Dropout	[0.0, 0.4]	0.239	0.260	0.0582
	Tradeoff parameter	$[10^{-2}, 10^2]_{\log}$	1.17	0.0562	0.0134
	Sinkhorn regularization	$[10^{-2}, 10^1]_{\log}$	0.0401	1.38	1.63
	Sinkhorn iterations	{5, ..., 30}	16	24	6
	JDOT α	$[10^{-2}, 10^1]_{\log}$	0.141	0.0424	0.0902
	JDOT β	[0.0, 2.0]	0.303	1.42	0.794

Table A.12: Same as Table A.7, but using Mean Teacher.

Architecture	Parameter	Search Space	Best run		
			sim-to-sim HPGe	sim-to-real LaBr ₃	sim-to-real NaI(Tl)
MLP	Learning rate	$[10^{-7}, 10^{-3}]_{\log}$	9.06e-4	5.36e-4	8.24e-4
	Batch size	$[64, 512]_{2^k}$	512	64	64
	Weight decay	$[10^{-7}, 10^{-3}]_{\log}$	7.45e-7	6.91e-6	6.83e-6
	Dropout	[0.0, 0.4]	0.0229	0.183	0.121
	Tradeoff parameter	$[10^{-2}, 10^3]_{\log}$	689	430	273
	EMA decay	[0.95, 0.9999]	0.9969	0.9559	0.9520
	Effective counts	$[10^2, 5 \times 10^4]_{\log}$	3.91e4	213	169
CNN	Learning rate	$[10^{-7}, 10^{-3}]_{\log}$	7.57e-4	2.42e-4	7.16e-4
	Batch size	$[64, 512]_{2^k}$	64	256	128
	Weight decay	$[10^{-7}, 10^{-3}]_{\log}$	7.36e-4	7.51e-7	2.51e-5
	Dropout	[0.0, 0.4]	0.365	0.0831	0.146
	Tradeoff parameter	$[10^{-2}, 10^3]_{\log}$	10.1	818	722
	EMA decay	[0.95, 0.9999]	0.9928	0.9634	0.9504
	Effective counts	$[10^2, 5 \times 10^4]_{\log}$	4.22e3	257	124
TBNN (Li <i>et al.</i>)	Learning rate	$[10^{-7}, 10^{-3}]_{\log}$	3.36e-4	9.62e-4	7.52e-4
	Batch size	$[64, 512]_{2^k}$	256	64	128
	Weight decay	$[10^{-7}, 10^{-3}]_{\log}$	8.01e-5	2.77e-4	1.84e-4
	Dropout	[0.0, 0.4]	0.0461	0.363	0.283
	Tradeoff parameter	$[10^{-2}, 10^3]_{\log}$	63.4	3.02	0.558
	EMA decay	[0.95, 0.9999]	0.9723	0.9523	0.9783
	Effective counts	$[10^2, 5 \times 10^4]_{\log}$	1.44e4	3.12e4	6.29e3
TBNN-LinEmb	Learning rate	$[10^{-7}, 10^{-3}]_{\log}$	8.51e-4	9.26e-4	8.64e-4
	Batch size	$[64, 512]_{2^k}$	512	128	64
	Weight decay	$[10^{-7}, 10^{-3}]_{\log}$	7.26e-6	7.13e-7	1.22e-4
	Dropout	[0.0, 0.4]	0.0878	0.0149	9.67e-3
	Tradeoff parameter	$[10^{-2}, 10^3]_{\log}$	8.58	322	3.83
	EMA decay	[0.95, 0.9999]	0.9814	0.9942	0.9526
	Effective counts	$[10^2, 5 \times 10^4]_{\log}$	3.92e4	395	224
TBNN-NonLinEmb	Learning rate	$[10^{-7}, 10^{-3}]_{\log}$	7.93e-4	8.15e-4	5.58e-4
	Batch size	$[64, 512]_{2^k}$	128	64	64
	Weight decay	$[10^{-7}, 10^{-3}]_{\log}$	1.76e-7	2.03e-6	2.36e-6
	Dropout	[0.0, 0.4]	0.0317	0.0454	0.0108
	Tradeoff parameter	$[10^{-2}, 10^3]_{\log}$	3.76	2.17	1.92
	EMA decay	[0.95, 0.9999]	0.9956	0.9591	0.9571
	Effective counts	$[10^2, 5 \times 10^4]_{\log}$	5.39e3	172	336

Table A.13: Same as Table A.7, but using SimCLR.

Architecture	Parameter	Search Space	Best run		
			sim-to-sim HPGe	sim-to-real LaBr ₃	sim-to-real NaI(Tl)
MLP	Learning rate	$[10^{-7}, 10^{-3}]_{\log}$	5.85e-4	3.21e-4	6.21e-4
	Batch size	$[64, 512]_{2^k}$	128	128	128
	Weight decay	$[10^{-7}, 10^{-3}]_{\log}$	2.00e-5	1.99e-4	5.92e-7
	Dropout	[0.0, 0.4]	0.124	0.101	0.311
	Tradeoff parameter	$[10^{-2}, 10^3]_{\log}$	670	41.2	74.8
	Temperature	$[10^{-2}, 0.5]_{\log}$	0.0918	0.499	0.491
	Projection layers	{1, 2, 3}	1	1	1
	Projection width	$[64, 1024]_{2^k}$	128	256	256
	Effective counts	$[10^2, 10^5]_{\log}$	3.02e4	4.69e3	1.84e3
CNN	Learning rate	$[10^{-7}, 10^{-3}]_{\log}$	1.40e-4	5.82e-6	9.08e-4
	Batch size	$[64, 512]_{2^k}$	512	256	256
	Weight decay	$[10^{-7}, 10^{-3}]_{\log}$	4.98e-7	6.44e-5	4.37e-6
	Dropout	[0.0, 0.4]	0.0990	0.262	0.103
	Tradeoff parameter	$[10^{-2}, 10^3]_{\log}$	95.7	472	2.63
	Temperature	$[10^{-2}, 0.5]_{\log}$	0.0664	0.173	0.449
	Projection layers	{1, 2, 3}	1	2	1
	Projection width	$[64, 1024]_{2^k}$	1024	1024	1024
	Effective counts	$[10^2, 10^5]_{\log}$	7.42e4	1.38e4	8.40e4
TBNN (Li <i>et al.</i>)	Learning rate	$[10^{-7}, 10^{-3}]_{\log}$	6.80e-4	8.78e-4	7.01e-4
	Batch size	$[64, 512]_{2^k}$	512	64	128
	Weight decay	$[10^{-7}, 10^{-3}]_{\log}$	5.44e-7	4.21e-7	5.65e-7
	Dropout	[0.0, 0.4]	0.0500	0.283	0.266
	Tradeoff parameter	$[10^{-2}, 10^3]_{\log}$	0.151	362	1.61
	Temperature	$[10^{-2}, 0.5]_{\log}$	0.0364	0.154	0.0821
	Projection layers	{1, 2, 3}	2	1	1
	Projection width	$[64, 1024]_{2^k}$	128	128	128
	Effective counts	$[10^2, 10^5]_{\log}$	2.29e4	5.98e3	7.16e4
TBNN-LinEmb	Learning rate	$[10^{-7}, 10^{-3}]_{\log}$	9.58e-5	9.24e-4	4.58e-4
	Batch size	$[64, 512]_{2^k}$	128	128	64
	Weight decay	$[10^{-7}, 10^{-3}]_{\log}$	3.62e-7	1.61e-6	7.28e-6
	Dropout	[0.0, 0.4]	0.208	0.159	0.142
	Tradeoff parameter	$[10^{-2}, 10^3]_{\log}$	0.418	1.55	278
	Temperature	$[10^{-2}, 0.5]_{\log}$	0.0469	0.201	0.443
	Projection layers	{1, 2, 3}	1	1	2
	Projection width	$[64, 1024]_{2^k}$	1024	64	128
	Effective counts	$[10^2, 10^5]_{\log}$	169	3.97e3	3.93e4
TBNN-NonLinEmb	Learning rate	$[10^{-7}, 10^{-3}]_{\log}$	9.06e-4	5.22e-5	7.50e-4
	Batch size	$[64, 512]_{2^k}$	512	64	128
	Weight decay	$[10^{-7}, 10^{-3}]_{\log}$	3.58e-7	3.57e-6	9.72e-7
	Dropout	[0.0, 0.4]	0.0785	0.166	0.207
	Tradeoff parameter	$[10^{-2}, 10^3]_{\log}$	36.8	13.2	177
	Temperature	$[10^{-2}, 0.5]_{\log}$	0.0738	0.430	0.495
	Projection layers	{1, 2, 3}	1	1	3
	Projection width	$[64, 1024]_{2^k}$	64	256	1024
	Effective counts	$[10^2, 10^5]_{\log}$	6.87e3	1.34e4	1.29e4

Table A.14: Calculated p -values from a one-sided Wilcoxon signed-rank test, testing the null hypothesis that UDA provides no improvement over the source-only baseline model. p -values below a significance threshold of 0.01 are bolded, indicating statistically significant improvement.

(a) Scenario: sim-to-sim (HPGe). Statistical significance tests compare testing APE score (UDA > source-only).

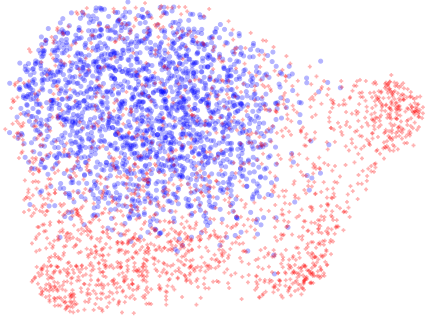
	MLP	CNN	TBNN (Li <i>et al.</i>)	TBNN-LinEmb	TBNN-NonlinEmb
ADDA	1.000	0.995	0.001	0.001	0.002
DAN	1.000	1.000	0.001	0.001	0.001
DANN	0.001	0.903	0.001	0.001	0.001
DeepCORAL	0.001	1.000	0.007	0.998	1.000
DeepJDOT	1.000	1.000	0.246	1.000	1.000
Mean Teacher	1.000	1.000	0.216	1.000	1.000
SimCLR	1.000	1.000	0.001	1.000	0.999

(b) Scenario: sim-to-real (LaBr₃). Statistical significance tests compare testing accuracy (UDA > source-only).

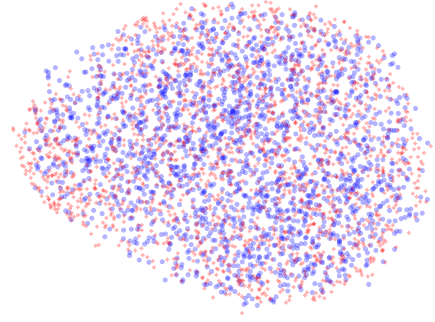
	MLP	CNN	TBNN (Li <i>et al.</i>)	TBNN-LinEmb	TBNN-NonlinEmb
ADDA	0.001	0.001	0.001	0.002	0.001
DAN	0.001	0.002	0.001	0.001	0.001
DANN	0.001	0.001	0.001	0.001	0.001
DeepCORAL	0.001	0.001	0.001	0.001	0.001
DeepJDOT	0.042	0.010	0.005	0.001	0.001
Mean Teacher	0.001	0.976	0.001	0.968	0.014
SimCLR	0.001	0.001	0.001	0.001	0.001

(c) Scenario: sim-to-real (NaI(Tl)). Statistical significance tests compare testing accuracy (UDA > source-only).

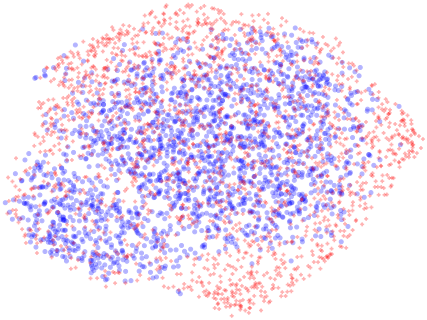
	MLP	CNN	TBNN (Li <i>et al.</i>)	TBNN-LinEmb	TBNN-NonlinEmb
ADDA	0.001	0.065	0.001	0.001	0.500
DAN	0.001	0.188	0.001	0.001	0.001
DANN	0.001	0.024	0.001	0.001	0.001
DeepCORAL	0.001	0.001	0.001	0.001	0.001
DeepJDOT	0.001	0.884	0.001	0.001	0.001
Mean Teacher	0.991	0.999	0.001	0.019	0.001
SimCLR	0.001	0.003	0.001	0.001	0.001



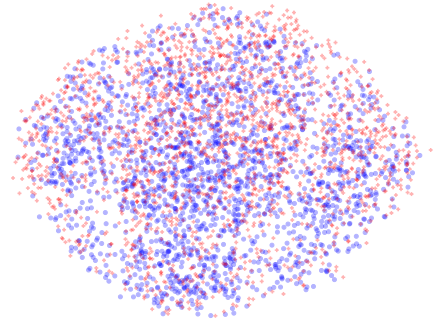
(a) Sim-to-sim HPGe scenario, source-only model.



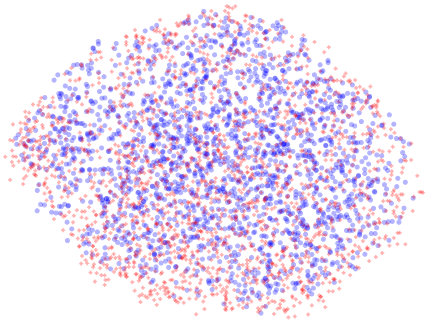
(b) Sim-to-sim HPGe scenario, ADDA model.



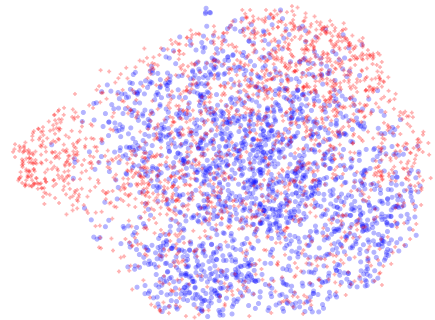
(c) Sim-to-sim HPGe scenario, DAN model.



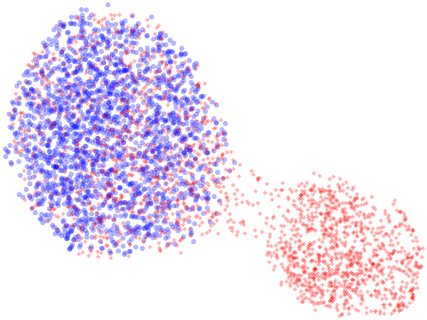
(d) Sim-to-sim HPGe scenario, DANN model.



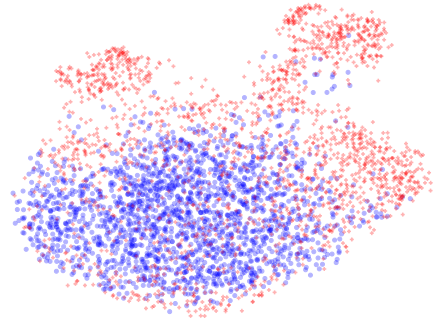
(e) Sim-to-sim HPGe scenario, DeepCORAL model.



(f) Sim-to-sim HPGe scenario, DeepJDOT model.

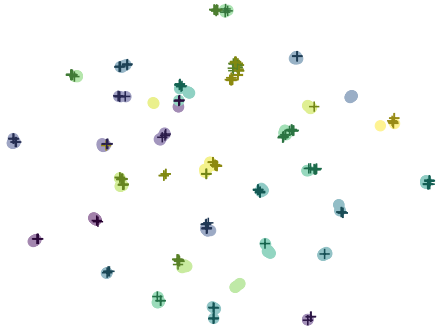


(g) Sim-to-sim HPGe scenario, Mean Teacher model.

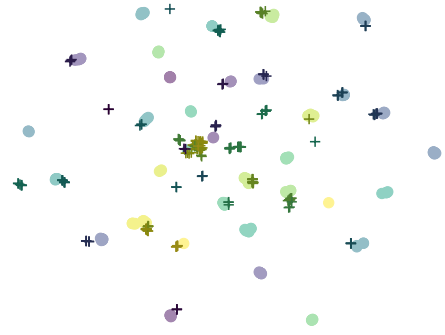


(h) Sim-to-sim HPGe scenario, SimCLR model.

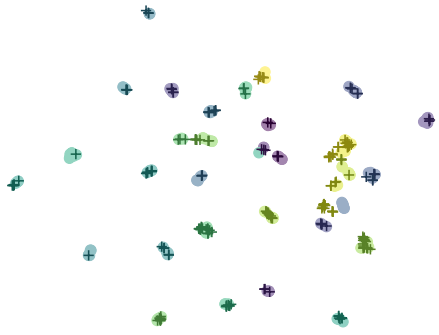
Figure A.3: UMAP visualizations of the feature extractor outputs for source spectra ('o' markers) and target spectra ('+' markers) for all UDA methods for the sim-to-sim domain adaptation scenario. Color indicates domain (blue = source, red = target).



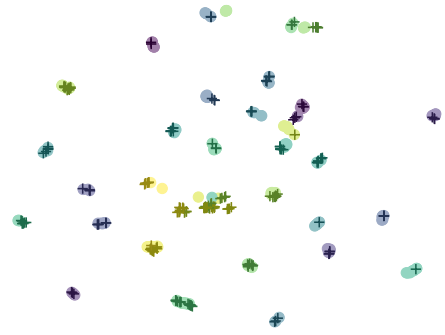
(a) Sim-to-real LaBr₃ scenario, source-only model.



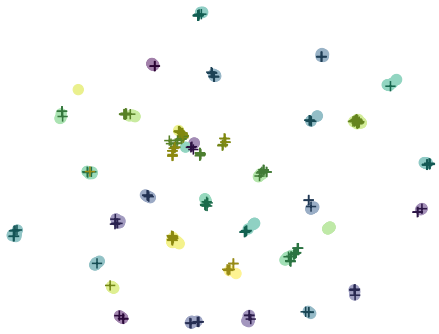
(b) Sim-to-real LaBr₃ scenario, ADDA model.



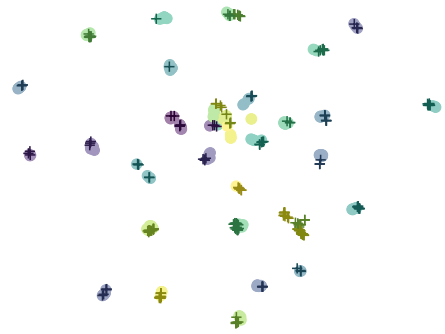
(c) Sim-to-real LaBr₃ scenario, DAN model.



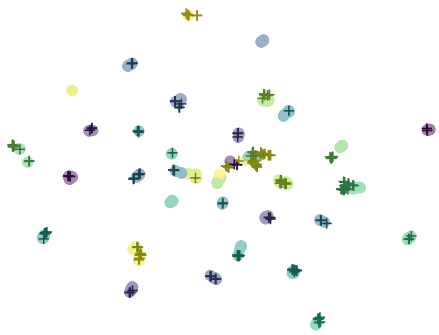
(d) Sim-to-real LaBr₃ scenario, DANN model.



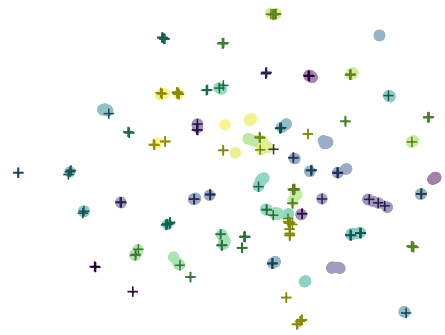
(e) Sim-to-real LaBr₃ scenario, DeepCORAL model.



(f) Sim-to-real LaBr₃ scenario, DeepJDOT model.

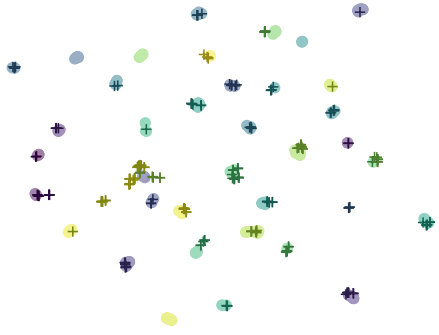


(g) Sim-to-real LaBr₃ scenario, Mean Teacher model.

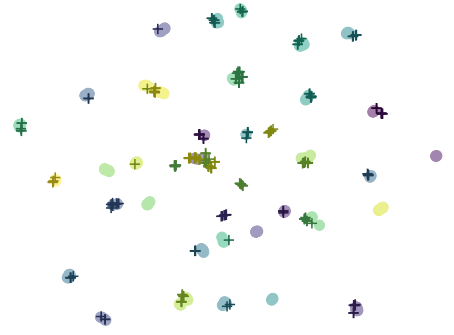


(h) Sim-to-real LaBr₃ scenario, SimCLR model.

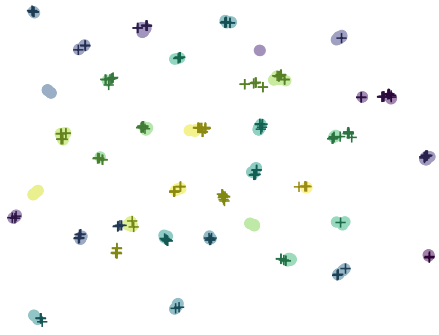
Figure A.4: Same as Fig. A.3, but for the sim-to-real LaBr₃ domain adaptation scenario. Color indicates class.



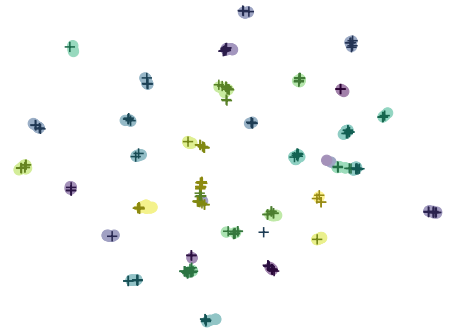
(a) Sim-to-real NaI(Tl) scenario, source-only model.



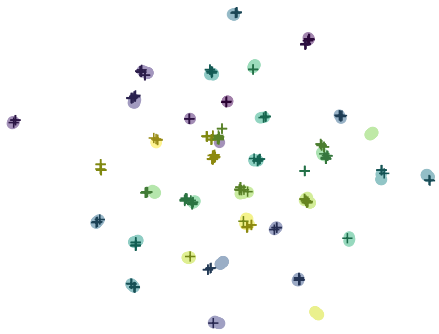
(b) Sim-to-real NaI(Tl) scenario, ADDA model.



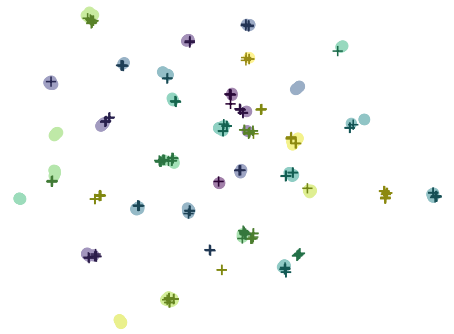
(c) Sim-to-real NaI(Tl) scenario, DAN model.



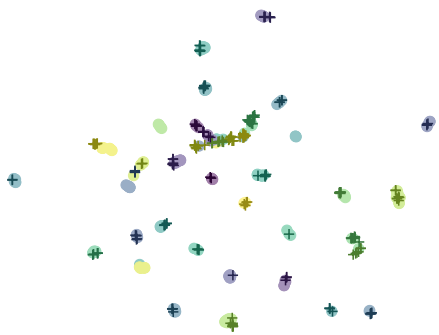
(d) Sim-to-real NaI(Tl) scenario, DANN model.



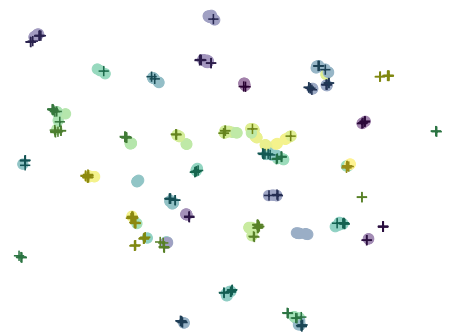
(e) Sim-to-real NaI(Tl) scenario, DeepCORAL model.



(f) Sim-to-real NaI(Tl) scenario, DeepJDOT model.



(g) Sim-to-real NaI(Tl) scenario, Mean Teacher model.



(h) Sim-to-real NaI(Tl) scenario, SimCLR model.

Figure A.5: Same as Fig. A.3, but for the sim-to-real NaI(Tl) domain adaptation scenario. Color indicates class.